Enhanced metanephric specification to functional proximal tubule enables toxicity screening and infectious disease modelling in kidney organoids

Jessica M. Vanslambrouck[1,2], Sean B. Wilson[1,2#], Ker Sin Tan[1#], Ella Groenewegen[1], Rajeev Rudraraju[4], Jessica Neil[4], Michelle Scurr[1], Sara E. Howden[1,2], Kanta Subbarao[4], Melissa H. Little[1,2,3*].

1. Murdoch Children's Research Institute, Flemington Rd, Parkville, VIC, Australia
2. Department of Paediatrics, The University of Melbourne, VIC, Australia.
3. Department of Anatomy and Neuroscience, The University of Melbourne, VIC, Australia.
4. Department of Microbiology and Immunology, The Peter Doherty Institute for Infection and Immunity, The University of Melbourne, VIC, Australia.

[#] Equal contribution

* Author for correspondence:

M.H.L.: +61 3 9936 6206; melissa.little@mcri.edu.au

Running title: Enhanced proximal tubules

Keywords: proximal tubule, pluripotent stem cell, kidney organoid, nephron patterning

Abstract

While pluripotent stem cell-derived kidney organoids represent a promising approach for the study of renal disease, renal physiology and drug screening, the proximal nephron remains immature with limited evidence for key functional solute channels. This may reflect early mispatterning of the nephrogenic mesenchyme or insufficient maturation. In this study, prolonged differentiation and modification of media conditions to enhance metanephric nephron progenitor specification resulted in the induction of nephrons containing elongated and aligned proximal nephron segments together with SLC12A1^{+} loops of Henle. Nephron proximal segments showed superior *HNF4A* gene and protein expression, as well as upregulation of key functional transporters, including *SLC3A1/2, SLC47A1*, and *SLC22A2*. The striking proximo-distal orientation of nephrons was shown to result from localised WNT antagonism originating from the centre of the organoid. Functionality of such transporters was evidenced by albumin and organic cation uptake, as well as appropriate KIM-1 upregulation in response to the nephrotoxicant, cisplatin. PT-enhanced organoids also possessed improved expression of receptors associated with SARS-CoV2 entry, rendering these organoids susceptible to infection and able to support viral replication without co-location of ACE2 and TMPRSS2. These PT-enhanced organoids provide an accurate model with which to study human proximal tubule maturation, inherited and acquired proximal tubular disease, and drug and viral responses.

Introduction

Chronic kidney disease (CKD) is an increasing global health and economic burden, attributed to 1.2 million deaths worldwide in 2017 alone (Collaboration, 2020). Most commonly associated with diabetes and high blood pressure, CKD also arises from genetic disorders, infections, and drug-induced toxicity. Key cellular targets of this disease are the kidney proximal tubules which possess a high metabolic activity making them acutely vulnerable to toxins and metabolic stress (Kirita, *et al.*, 2020). In mammals, this highly specialised segment of the nephron performs the bulk of kidney reabsorption and secretion via three distinct functional and anatomical segments: the convoluted (S1 and S2) proximal tubule segments and the straight (S3) segment that traverses the cortico-medullary boundary. Of these, S1 exhibits the highest capacity for solute, sodium, amino acid and fluid transport (Zhuo and Li, 2013). The dramatic effect that proximal tubule injury has on body homeostasis underpins the complexities faced in CKD management. While current CKD treatment options such as dialysis and transplantation can be life-prolonging, they are complicated by high morbidity rates and donor organ shortages (Collaboration, 2020). These treatment deficits are further confounded by our limited understanding of disease mechanisms due to a lack of accurate human-relevant disease models.

We and others have established robust protocols for the directed differentiation of human pluripotent stem cells to kidney progenitors capable of self-organisation into complex kidney structures (Freedman, *et al.*, 2015; Morizane, *et al.*, 2015; Taguchi, *et al.*, 2014; Toyohara, *et al.*, 2015). These kidney organoids show a remarkable transcriptional similarity to the developing human kidney (Combes, *et al.*, 2019; Howden, *et al.*, 2021; Subramanian, *et al.*, 2019; Wu, *et al.*, 2018), most closely resembling human trimester 1 development by 3- 4 weeks of culture (Takasato, *et al.*, 2015) and possessing many of the structures expected within fetal kidney *in vivo*, including glomeruli, nephrons, stroma and vasculature (Takasato, *et al.*, 2016). However, nephron patterning and segmentation remain noticeably immature in kidney organoids, even in comparison to the fetal organ. This is particularly noticeable in the proximal tubule segment of the nephron. While there is clear expression of *HNF4A*, responsible for driving early proximal patterning (Marable, *et al.*, 2020), and characteristic apical co-localisation of the CUBILIN-MEGALIN complex, existing kidney organoid protocols fail to promote the expression and maturation of the functional solute channels that define each proximal tubule subsegment (Wu, *et al.*, 2018; Wilson, *et al.*, 2021). Critically, expression

levels of the principal water transporting channel, AQP1, the organic anion transporters (OATs), and the organic anion transporters (OATs) are all low (Wilson, *et al.*, 2021) This represents a considerable obstacle to the modelling of proximal tubular disorders or the screening of drugs or toxins using kidney organoids.

Suboptimal proximal tubule maturation in organoids may be regarded as a problem of inappropriate anteroposterior/mediolateral patterning, suboptimal maintenance of progenitor identity or incomplete maturation. In response to distinct temporospatial signalling, the permanent (metanephric) kidney arises during human embryogenesis as the final of three embryonic excretory organs, developing sequentially from specific rostrocaudal regions of the intermediate mesoderm located between the lateral plate mesoderm and paraxial somatic mesoderm (Dressler, 2009). Metanephric kidney development in humans commences during weeks 4 – 5 (de Bakker, *et al.*, 2019) with the first nephrons appearing by week 6 – 7. In mouse and human, nephron formation involves a mesenchyme to epithelial transition (MET) from a population of $SIX2^{+}$ nephron progenitors that form a cap mesenchyme around the tips of the branching collecting duct (Kobayashi, *et al.*, 2008; Lindstrom, *et al.*, 2018). However, preceding metanephric development is the formation of two more rostral transient excretory organs; the pronephros (present in human from gestation week 3 - 4) and the mesonephros (present in human from gestation week 4 – 10). While the mammalian pronephros is highly rudimentary, mesonephric nephrons also arise via MET and show similar patterning and segmentation to metanephric nephrons, albeit with less definitive distal tubule segments (Georgas, *et al.*, 2011; Mugford, *et al.*, 2008; Tiedemann, *et al.*, 1987). The mesonephros functions as the principle excretory organ until week 8 after which time it regresses suggesting that mesonephric tubular function is less advanced compared to the metanephros (reviewed in de Bakker, *et al.*, 2019) .

Using fluorescent reporter lines and lineage tracing in human kidney organoids, we have confirmed both the presence of a $SIX2^{+}$ nephron progenitor population and the contribution of these cells to nephrogenesis via MET in kidney organoids (Howden, *et al.*, 2019; Vanslambrouck, *et al.*, 2019). However, given the short duration of ours and other organoid protocols (reviewed in Little and Combes, 2019), the possibility exists that we are modelling mesonephric rather than metanephric nephrogenesis, potentially contributing to poor proximal tubule patterning and maturation. In agreement with this notion, previous studies have observed variations in anteroposterior patterning of the intermediate mesoderm during hPSC

differentiation *in vitro* (Taguchi, *et al.*, 2014; Takasato, *et al.*, 2015; Tsujimoto, *et al.*, 2020). The influence of mediolateral signalling cues during mesodermal patterning further complicate iPSC differentiation, with inappropriate signalling likely to influence paraxial or lateral plate mesoderm proportion, thus reducing effective nephron generation.

An alternate contributing factor is suboptimal maintenance of progenitor identity during iPSC differentiation and organoid generation. Several media have been described that are able to support the maintenance of isolated nephron progenitors *in vitro* (Brown, *et al.*, 2015; Li, *et al.*, 2016; Tanigawa, *et al.*, 2015; Tanigawa, *et al.*, 2016). While each media contains low levels of canonical WNT activity and FGF2/9, the inclusion of a variety of TGFβ superfamily agonists (BMP4, BMP7, Activin A) and antagonists (A83-01, LDN193189), NOTCH inhibition (DAPT), and other growth factors (TGFα, IGF1/2, LIF) varies between media. These media have been referred to as NPEM, NPSR, and CDBLY based upon their components, with all studies reporting maintenance of a SIX2-expressing nephron progenitor population in culture across time (Brown, *et al.*, 2015; Li, *et al.*, 2016; Tanigawa, *et al.*, 2016). However, the resulting nephrons formed after subsequent nephron induction showed distinct differences in nephron patterning. In NPEM, the inclusion of LDN193189 (inhibitor of BMP receptor-mediated SMAD1/5/8) supported tubular patterning but not formation of glomeruli (Brown, *et al.*, 2015). In contrast, the addition of LIF and either dual-SMAD inhibition (LDN193189 and A83-01) or NOTCH inhibition (DAPT) resulted in the formation of nephrons with podocytes but distinct nephron morphologies (Li, *et al.*, 2016; Tanigawa, *et al.*, 2016). While proximodistal nephron patterning in mouse has previously been shown to be influenced by relative Wnt, Bmp, and Notch signalling in mouse (Lindstrom, *et al.*, 2015), these data suggest that distinct nephron progenitor states may show varying competence for different nephron segments, or that distinct SIX2 populations give rise to different regions of the nephron.

In the current study, we sought to understand whether anteroposterior/mediolateral patterning, or shifts in commitment state of the nephron progenitors, could influence ultimate proximal tubule identity and maturation. We initially sought to maximise patterning to a posterior metanephric $SIX2^{+}$ nephron progenitor population by extending the duration of mesodermal patterning, simultaneously suppressing MET and supporting nephron progenitor expansion using previously described media (Li, *et al.*, 2016; Tanigawa, *et al.*, 2016). Compared to standard pluripotent stem cell-derived kidney organoids, prolonged monolayer iPSC differentiation in modified CDBLY nephron progenitor maintenance media (Tanigawa, *et al.*,

2016) specified nephron progenitors with improved metanephric identity without influencing anteroposterior/mediolateral patterning. These progenitors formed strongly proximalised, elongated, and spatially aligned nephrons, with striking proximo-distal nephron orientation resulting from localised WNT antagonism. Proximal tubules possessed substantially improved maturation, evidenced by upregulation of key solute channels and transporters. This was strengthened by their functional uptake of albumin, organic cations, and cisplatin, eliciting appropriate KIM-1 upregulation. Improved proximal tubules of these enhanced organoids also showed increased expression of key viral entry factors for SARS-CoV-2 compared to previous protocols, validating the proximal tubule as the primary target for viral entry despite a complete separation of the viral receptor, ACE2 (proximal tubule), and the viral entry cofactor, TMPRSS2 (distal tubule). Taken together, this study suggests a requirement for optimal nephron progenitor commitment for appropriate proximal tubule identity. Proximal tubule-enhanced kidney organoids represent an improved model of the human nephron with likely applications for infectious and genetic disease research, as well as evaluation of drug responses.

Results

Prolonged monolayer culture and delayed nephron induction supports nephron progenitors

As noted previously, optimisation of nephron progenitor maintenance *in vitro* has been investigated by a range of studies using murine and human pluripotent stem cell-derived nephron progenitors (Brown*, et al.*, 2015; Li*, et al.*, 2016; Tanigawa*, et al.*, 2016). While all studies reported maintenance of nephron progenitors, variations were evident with respect to the final patterning of resulting nephrons following induction. Given the clear influence that initial differentiation conditions and timing can have on nephron progenitor survival and subsequent nephron patterning, we hypothesised that expanding our nephron progenitor population whilst delaying nephron initiation may create a more metanephric population leading to organoids with improved patterning and PT maturation. We have previously shown that SIX2 expression is not detected until day 10 of pluripotent stem cell differentiation (Howden*, et al.*, 2019). Hence, the initial monolayer differentiation phase was prolonged to between 12 – 14 days, along with culture in either of two previously defined NP maintenance media, NPSR (Li*, et al.*, 2016) and CDBLY (Tanigawa*, et al.*, 2016) from day 7, which represents the point of intermediate mesoderm commitment (Takasato*, et al.*, 2015; Takasato*, et al.*, 2014) (Figure 1A). Compared to control media (TeSR-E6; E6), both NPSR and CDBLY prevented spontaneous epithelialisation of the monolayer (Figure 1B). However, only CDBLY preserved the nephron-forming capacity of the progenitor cells following micromass formation and induction of nephrogenesis with a pulse of canonical WNT signalling (Figure 1B). By contrast, very little epithelialisation and poor nephron commitment was observed after culture in NPSR (Figure 1B).

The prevention of spontaneous differentiation while preserving the nephrogenic capacity of the NP cells was found to be primarily a response to the presence of CDB (CHIR, DAPT, BMP7), with omission of LIF, Y27632, as well as the basal media component TGFα, found to produce a similar result with respect to growth, morphology and nephron segmentation compared to CDBLY (Figure 1C). The inhibition of monolayer epithelialisation with preserved nephrogenic capacity was found to be consistent at monolayer differentiation lengths tested (10, 12, 13 and 14 days) (Supplementary Fig 1A). However, a monolayer differentiation length of 12 – 13 days produced more consistent nephrogenesis between experiments, with 14 days leading to

frequent detachment of the differentiating monolayer. Subsequent studies proceeded using prolonged culture in CDBLY noting the inclusion of an increased concentration of BMP7 (10ng/mL; CDBLY2) which improved reproducibility of organoid nephrogenesis between organoids compared to standard CDBLY (5ng/mL BMP7) (Supplementary Figure 1B). This modified differentiation protocol is detailed in Figure 1A.

Quantitative RT-PCR (qRT-PCR) of the extended monolayer differentiations in CDBLY2 confirmed an improved metanephric gene expression profile compared to standard differentiations performed in parallel (7 day protocol in E6 (Takasato*, et al.*, 2016; Howden*, et al.*, 2019)) (Figure 1D). Extended CDBLY2 monolayers showed a significant increase in *SIX1*/*SIX2* (self-renewing to committed NPs) and *WNT4* (primed to committed NPs), while *DAPL1* (self-renewing and primed NPs) was increased without significance and no change was observed in *TMEM100* (self-renewing NPs). This suggested that the extended protocol promotes a primed, rather than self-renewing, NPC population (Hochane*, et al.*, 2019; Lindstrom*, et al.*, 2018; Lindstrom*, et al.*, 2018). Extended differentiation in CDBLY2 was not found to alter mediolateral patterning, with no change in paraxial mesodermal marker *PARAXIS* and unchanged or increased expression of intermediate mesoderm markers *HOXD11*, *LHX1*, and *GATA3* (Mugford*, et al.*, 2008).

Extended monolayer culture induces SIX2-derived proximalised nephrons

Lineage tracing studies in mouse have shown that nephrons are derived entirely from Six2+ nephron progenitors (Kobayashi*, et al.*, 2008), with histological studies suggesting a similar developmental process in human (Lindstrom*, et al.*, 2018; Lindstrom*, et al.*, 2018) ((Kobayashi*, et al.*, 2008). Using a $SIX2^{Cre/Cre}$:$GAPDH^{dual}$ lineage tracing line, in which SIX2 expression induces a permanent GFP/mCherry switch, we have previously shown that kidney organoid nephrons contain cells derived from $SIX2^{+}$, at also $SIX2^{-}$, progenitor cells, resulting in a chimeric appearance (Howden*, et al.*, 2019). To confirm and compare the competence of the metanephric progenitor-enriched monolayer differentiation to contribute to nephron formation, organoids were generated from our extended and the standard differentiation protocol using the $SIX2^{Cre/Cre}$:$GAPDH^{dual}$ lineage tracing line. Immunofluorescence of extended protocol organoids confirmed an increase in the contribution of SIX2-derived cells within the forming nephrons, including $NPHS1^{+}$ podocytes, LTL^{+} proximal tubules and E-$CADHERIN^{+}$ distal tubules (Figure 2A). Using flow cytometry, SIX2-derived cell contribution

to EPCAM^{+} nephrons was significantly higher in organoids derived from the metanephric progenitor-enriched monolayers compared to standard organoids, suggesting improved metanephric identity of prolonged monolayers exposed to CDBLY2 (Figure 2B).

The patterning of these increasingly SIX2-progenitor nephrons was examined using a range of markers for podocytes, proximal, and distal tubules, indicating clear proximo-distal segmentation and a large proportion of proximal tubule (Figure 2C), with little to no GATA3 expression marking ureteric epithelialisation (Figure 2D). Organoids also displayed aligned nephrons, with a central ring of glomeruli and elongated proximal tubules radiating outwards. This unique organoid morphology was observed in organoids derived from 6 different iPSC lines with or without gene editing and from male or female iPSC sources (3 examples evidenced in Supplementary Figure 1C). The proportion of proximal tubule cells in organoids derived from extended monolayer culture with CDBLY2 was compared to those derived from the standard differentiation protocol (7 days differentiation, cultured in E6 (Howden*, et al.*, 2019)). Organoids were generated using the HNF4A^{YFP} iPSC reporter line which reports the formation of proximal tubule (Vanslambrouck*, et al.*, 2019). This revealed up to 6.2 times higher average proportions of HNF4A^{YFP+} proximal tubule cells in organoids derived from the extended monolayer protocol compared to the standard protocol (Figure 2D). These results confirmed the use of extended monolayer differentiation combined with progenitor-supportive media, CDBLY2, as an effective method of generating proximal tubule enhanced (PT-enhanced) kidney organoids.

Transcriptional profiling of PT-enhanced organoids confirms improved proximal tubule patterning and maturation

To gain deeper insight into the complexity and maturity of cells within this extended protocol, both as the stage of monolayer (day 13) and within the resulting PT-enhanced organoids, transcriptional profiling was performed using multiplexed single cell RNA sequencing (scRNAseq) and antibody-based cell barcoding. To account for variation, libraries were generated from 4 separate differentiated monolayers representing distinct starting pools of iPSCs (CRL1502.C32) that were used to generate 4 separate batches of organoids (Figure 3A). Cells from the 4 replicates (both at day 13 [D13] monolayer stage, prior to organoid formation, and day 14 of organoid culture [D13+14]) were barcoded using hashing antibodies before being

pooled. This approach produced a single library for each timepoint (sample) which could be later deconvoluted to retrieve replicate information.

The resulting D13 and D13+14 pooled replicate libraries resolved 19,956 and 15,852 individual cell transcriptomes per timepoint, respectively. UMAP plots showed the resolution of distinct clusters for both D13 monolayers and resulting PT-enhanced (D13+14) organoids (Figure 3B). Gene expression analyses confirmed the expression of a range of markers for mesenchymal cell states pre-kidney organogenesis in D13 monolayers, as well as markers of proximodistal patterning, stroma, and endothelium in D13+14 organoids (Supplementary Figure 2; Supplementary Tables 1 and 2). To enable unbiased comparisons of kidney cell type proportions and gene expression levels of D13 and D13+14 samples with published stem cell-derived and reference kidney datasets, datasets were analysed using *DevKidCC* (Wilson*, et al.*, 2021). The *DevKidCC* package enables robust classification of novel developing human or stem cell-derived kidney organoid datasets without the need for integration or prior dimensional reduction or clustering. Using the *ComparePlot* function, the D13 and D13+14 samples were directly compared with respect to their kidney cell proportions. This confirmed distinct differences in kidney cell populations, but consistency between the 4 replicates within each sample (Figure 3C and Supplementary Figure 3A). As anticipated, over 90% of cells within the D13 monolayer differentiations were classified as NPC or NPC-like, with a small contribution of cells classified as early nephron. In contrast, D13+14 organoids possessed a range of proximal and distal nephron cell types, as well as renal corpuscle cell types. Early proximal tubule (EPT) formed the largest proportion of organoid nephron cell types (51% average across 4 samples), while two replicates possessed a small (<5%) fraction of maturing PT cells. By contrast, previous studies of the standard organoid protocol (Takasato et al, 2015) show on average <25% EPT and no PT.

To gain in-depth understanding of the impact of prolonged monolayer culture in CDBLY2 on the identity and maturity of the resulting cell types, we firstly used *DevKidCC* to compare the expression of cell type-specific markers in D13 and D13+14 samples to published stem cell-derived and reference fetal kidney datasets (Figure 3D-F). Analysis of the NPC population within D13 samples confirmed strong gene signatures for committed NPCs (*SIX1, SIX2*, and *LYPD1*) and the metanephric HOX code (*HOXC10/11, HOXA11*, and *HOXD11*) compared to relevant published monolayer and nephrogenic-stage differentiations (Subramanian*, et al.*, 2019; Wu*, et al.*, 2018; Low*, et al.*, 2019; Tran*, et al.*, 2019) that better emulated the mixed

reference dataset of week 11, 13, 16, and 18 human fetal kidneys (Hochane, *et al.*, 2019; Tran, *et al.*, 2019; Holloway, *et al.*, 2020). PT-enhanced organoids derived from these D13 monolayer differentiations possessed high and abundant expression of a range of proximal nephron markers in their EPT population (Figure 3E). These included genes encoding several membrane proteins critical for proximal tubular transport of proteins and amino acids (*CUBN, LRP2, SLC3A1*, and *SLC3A2*), as well as auxiliary proteins and transcription factors required for transporter regulation and functionality, such as *AMN*, *AGT*, and *HNF4A*. This gene signature showed remarkable congruence to reference human fetal kidney and improved PT identity compared to existing published kidney organoid datasets (Czerniecki, *et al.*, 2018; Harder, *et al.*, 2019; Kumar, *et al.*, 2019) (Figure 3E).

An important anatomical feature of the mature PT is its segmentation into functionally and morphologically distinct regions defined as the S1/S2 convoluted tubule segments and the S3 straight segment. In addition to differences in proliferation characteristics and protein synthesis (Zhuo and Li, 2013; Avissar, *et al.*, 1994), the convoluted and straight segments display distinct differences in solute handling to accommodate the declining concentration of solutes as the ultrafiltrate passes through the nephron. As such, early S1 – S2 convoluted segments express low-affinity/high-capacity transporters, with a gradual transition to high-affinity/low-capacity transporters in the later S3 straight segment (Palacin, *et al.*, 2001; Schuh, *et al.*, 2018; Verrey, *et al.*, 2005). To determine whether the PTs of enhanced organoids show evidence of this segmentation, PT clusters from the 4 integrated D13+14 replicate datasets were isolated and re-clustered, resolving 4740 PT cells across 6 distinct clusters (Supplementary Figure 3B). The PT population was analysed for the expression of segment-specific PT markers with critical functional roles, including solute carriers for ions (*SLC34A1*/NPT2 (Fenollar-Ferrer, *et al.*, 2015) expressed in S1>S2), glucose (*SLC2A2*/GLUT2 and *SLC5A2*/SGLT2 expressed in S1>S2; *SLC2A1*/GLUT1 and *SLC5A1*/SGLT1 expressed in S2<S3 (Hummel, *et al.*, 2011; Rahmoune, *et al.*, 2005; Wood and Trayhurn, 2003)), amino acids (*SLC7A9*/b(0,+)AT transporter of cystine, aspartate, and glutamate expressed in S1/S2 > S3 (Nagamori, *et al.*, 2016)), and cationic drugs/toxins (*SLC47A1*/MATE1 expressed in S1/S2 > S3 (Otsuka, *et al.*, 2005)), as well as *AKAP12* (involved in cell cycle regulation, expressed in S2<S3 (Vogetseder, *et al.*, 2008) and *GPX3* (glutathione peroxidase; secreted antioxidant synthesised in S1/S2>S3 (Avissar, *et al.*, 1994)). UMAP plots revealed the largely opposing distributions of cells expressing S1>S2 and S2>S3 gene signatures (Supplementary Figure 3C). Cells expressing S1>S2 convoluted PT markers (*SLC34A1*/MATE1, *SLC2A2*/GLUT2, and *SLC5A2*/SGLT2)

were predominantly located in clusters 0, 3, and the lower portion of cluster 4, whereas cells expressing S2<S3 straight PT markers (*AKAP12*, *SLC2A1*/GLUT1, and *SLC5A1*/SGLT1) were primarily within clusters 1, 2, and the upper portion of cluster 4. When analysed for markers that exhibit a gradient of expression along the length of the nephron (S1/S2>S3), UMAP plots for each gene revealed a similar graded expression pattern, with a higher concentration of positive cells within the S1>S2 cluster (0) and decreasing in prevalence within S2<S3 clusters (0, 2) (Supplementary Figure 3C). Together this suggested that, despite the low expression of some markers indicating PT immaturity, the PTs of enhanced kidney organoids show evidence of separation into the 3 distinct anatomical PT segments.

Comparison between organoids is confounded by the inherent variability of different organoid protocols, technical variables and individual cell line characteristics. To minimise potential bias when comparing cell maturation, PT-enhanced organoid scRNASeq data was compared to that of an iPSC line-matched organoid of equivalent organoid age (day 11 – 12 of organoid culture), generated using our standard protocol but with equivalent techniques (Howden*, et al.*, 2019). Libraries from the PT-enhanced and standard organoid samples resolved 6737 and 1879 cells, respectively. Datasets were integrated prior to quality control measures to enable direct comparison of PT maturation and UMAP plots confirmed the resolution of distinct kidney cell clusters for both samples (Supplementary Figure 3D). Violin plots of the PT cluster alone in integrated datasets confirmed that the PT-enhanced organoid dataset possessed higher and more abundant expression of genes critical for PT functionality compared to the standard organoid (Figure 3Fi-ii). Examples included genes encoding membrane transporters CUBILIN/*CUBN* and MEGALIN/*LRP2* (important for protein uptake (Nielsen*, et al.*, 2016)), heavy-chain subunit solute carriers rBAT/*SLC3A1* and 4F2/*SLC3A2* (required for heteromer formation and amino acid transport by SLC7 family members (Kowalczuk*, et al.*, 2008)), light-chain subunit solute carriers y+LAT-1/*SLC7A7* and LAT2/*SLC7A8* (responsible for regulating intracellular amino acid pool via basolateral efflux of basic and neutral amino acids for transport systems y+L and L, respectively (Kanai*, et al.*, 2000; Verrey, 2003)), and solute carriers critical for PT metabolism and drug transport (G6PT1/*SLC37A4* and MATE1/*SLC47A1* (Lee*, et al.*, 2015)). Several auxiliary proteins essential for correct apical localisation and transporter functionality also showed higher expression in the PT-enhanced dataset, including *AMN* (Amnionless), *ACE2,* and *TMEM27* (Collectrin) (Kowalczuk*, et al.*, 2008; Camargo*, et al.*, 2009; Fyfe*, et al.*, 2004; Ahuja*, et al.*, 2008) (Figure 3Fi). Expression of genes encoding drug transporters *SLC22A2* (OCT2) and *SLC22A6* (OAT1) were low in both

conditions (Figure 3Fii). However, the PT-enhanced condition resulted in higher expression of both transporters compared to standard.

To investigate PT maturation further, an unbiased ToppFun GO Molecular Function analysis was performed on genes that were significantly differentially expressed within the PT cluster of PT-enhanced compared to standard organoids (945 input genes). This analysis revealed key differences in genes involved in cell metabolism (Figure 3G and Supplementary Figure 3E). PT-enhanced organoid cells within the PT cluster showed increased expression of genes related to fatty acid metabolism and its regulation, such as *PPARG*, *FABP3*, *PRKAA2*, and *FAT1* (Figure 3G). Given the known reliance of mature PT cells on fatty acid metabolism *in vivo* (reviewed in Zhuo and Li, 2013), this gene signature was suggestive of a more mature metabolic profile in enhanced compared to standard organoid PT cells. Taken together, these comprehensive scRNASeq analyses confirmed an increased abundance and relative maturation of PT within this extended protocol. Analyses of D13 monolayers suggests this higher-order PT patterning arises from improved NPC identity at the point of metanephric specification.

Mature expression and localisation of proximal tubule proteins enables nephron functionality

To establish the maturity of PTs within enhanced organoids at a protein-level, D13+14 organoids were examined via immunofluorescence for expression and correct cellular localisation of PT function markers (Figure 4A). Within LTL-positive tubules, organoids expressed a range of critical proteins, including membrane transporters CUBILIN (CUBN), MEGALIN (MEG) and SLC6A19 (Figure 4Ai – ii), as well as the nuclear transcription factor, HNF4A (Figure 4Aiii). This strong expression and apical cellular localisation of transporters was suggestive of nephron functionality. To test this, we firstly performed multiple substrate uptake assays specific to proximal tubules (Figure 4B). PT-enhanced organoids demonstrated a capacity for uptake of fluorescently labelled albumin (TRITC-albumin) specifically into MEG-positive proximal tubules, indicative of CUBN-MEG transport function (Figure 4Bi). In addition, these PTs also demonstrated robust uptake of 4′,6-diamidino-2-phenylindole (DAPI); an effective probe for evaluation of the PT-specific SLC47 family of organic cation/H^+ antiporters, MATE-1 (Multidrug and Toxin Extrusion Protein 1) and MATE2-K (Multidrug and Toxin Extrusion Protein 2K) (Yasujima*, et al.*, 2010) (Figure 4Bii). The uptake of DAPI by PT cells was successfully inhibited via pre-treatment of organoids with Cimetidine, a cation

transporter inhibitor, supporting the specificity of transport activity, while the absence of DRAQ7 staining excluded the possibility of DAPI uptake in PTs due to cell death.

Having established albumin and organic cation transport capacity, we next assessed the response of PT-enhanced organoids to nephrotoxic insult. Several recent studies have explored the suitability of kidney organoids as a human-relevant model of cisplatin-induced nephrotoxicity (Freedman, *et al.*, 2015; Morizane, *et al.*, 2015; Takasato, *et al.*, 2015), a common complication that limits usage of this chemotherapeutic agent (Ozkok and Edelstein, 2014; Yao, *et al.*, 2007). The biomarker KIM-1 is sensitive for early detection of PT injury in humans and animals (Abdelsalam, *et al.*, 2018; Chiusolo, *et al.*, 2010; Sasaki, *et al.*, 2011; Shinke, *et al.*, 2015; Vaidya, *et al.*, 2010) and has been shown to increase in response to cisplatin in kidney organoids, despite conflicting reports regarding its PT-specificity (Morizane, *et al.*, 2015; Takasato, *et al.*, 2016; Digby, *et al.*, 2020). This discrepancy may arise from immature expression of the predominant cisplatin transporters, particularly SLC22A2/OCT2 (Digby, *et al.*, 2020) combined with heterogeneity in cisplatin uptake mechanisms. Re-analysis of our existing D13+14 scRNASeq data revealed low-level expression of transporters for both cisplatin influx and efflux (Supplementary Figure 3F), including *SLC22A2*/OCT2 previously reported to show low expression in organoids (Digby, *et al.*, 2020), suggestive of cisplatin transport capacity. To confirm the functionality of these transporters and appropriate injury response by PTs, D13+14 organoids were exposed to 20 μM cisplatin for 24 hours. Immunofluorescence analysis revealed upregulation of KIM-1 protein expression within LTL-positive PTs of enhanced organoids compared to PBS-treated controls (Figure 4C). This was supported by a significant increase in the expression of *HAVCR1* relative to *HNF4A* ($P = 0.003$) (Figure 4D). Together, these data confirmed efficient cisplatin uptake and expected injury response.

Radial nephron patterning and alignment is associated with localised WNT antagonism

Of interest was the characteristic radial patterning observed in all PT-enhanced organoids, where tubules align with their glomeruli towards the centre of the organoid and distal SLC12A1+ segments towards the organoid periphery (refer to Figure 2B). This distinct morphology and patterning was found to be strongly driven by the intensity and duration of canonical WNT signalling (induced by CHIR) during the initial monolayer differentiation conditions (Figure 5). While exposure of the iPSC monolayer to WNT signalling for 5 days

prior to CDBLY2 promoted radially-aligned PTs, exposure to the iPSCs to a reduced duration of WNT signalling (4D x 7µM), which more closely resembled standard organoid protocols (Takasato*, et al.*, 2015; Howden*, et al.*, 2019; Vanslambrouck*, et al.*, 2019) led to the generation of evenly distributed patterned nephrons surrounding a GATA3-positive CNS/ureteric epithelial network (Figure 5A). Closer histological examination of PT-enhanced organoids revealed the nephron glomeruli to be aligned around a central interstitial core that differentiated into Alcian blue-positive cartilage with prolonged organoid culture (Figure 5B).

Previous studies have suggested that proximo-distal patterning is controlled by Wnt/β-catenin signalling along the nephron axis, with lower WNT signalling leading to improved formation and maturation of the proximal nephron (Lindstrom*, et al.*, 2015). In agreement with this, WNT inhibition has been observed to promote podocyte commitment in PSC cultures (Yoshimura*, et al.*, 2019). These findings suggested that the central pre-cartilage core of the PT-enhanced organoids may be expressing a localised WNT antagonist influencing nephron patterning. This was supported by re-analysis of our organoid scRNASeq data, confirming the expression of WNT antagonists in D13+14 organoids (Supplementary Figure 4B). Secreted Frizzled-related Protein 2 (sFRP2), a gene with known expression and involvement in developing kidney (Lescher*, et al.*, 1998; Yoshino*, et al.*, 2001), was the most abundantly expressed antagonist and displayed the highest expression levels in the cartilage clusters (clusters 2 and 5), followed by stroma (Supplementary Figure 3A).

To test whether localised WNT antagonism has a functional impact on nephron development we recreated a signalling gradient using agarose beads soaked in WNT inhibitor (10µM IWR-1). Following the 7 day (standard) differentiation protocol, iPSC-derived kidney progenitors were bioprinted and cultured to create rectangular patch organoids (Lawlor*, et al.*, 2021). Following 5 days of organoid culture (D7+5) and the formation of renal vesicles, IWR-1-soaked or control (PBS-soaked) beads were added to the centre of the organoids where they made contact with the early epithelial structures (Supplementary Figure 4B). After 9 days of organoid culture, organoids with IWR-1-soaked beads exhibited visible differences in the morphology of structures surrounding the beads compared to controls (organoids with PBS-soaked beads) (Supplementary Figure 3C). This became more apparent when these organoids were stained via immunofluorescence (Figure 5D). In organoids exposed to PBS-soaked beads, beads were in contact with a mixture of proximal and distal EPCAM-positive nephron epithelium, as well as NPHS2-positive podocytes of glomeruli (Figure 5Ci). In contrast, IWR-

1-soaked beads were predominantly surrounded by glomeruli, with few distal (LTL-negative/EPCAM-positive) visible overall (Figure 5Cii). This supports a localised WNT antagonism being responsible for the nephron directionality and alignment in PT-enahnced organoids.

PT-enhanced organoids represent an improved model for SARS-CoV-2 pathogenesis research

Kidney organoids have previously proven useful to model inherited, early-onset kidney disease (Freedman, *et al.*, 2015; Czerniecki, *et al.*, 2018; Cruz, *et al.*, 2017; Forbes, *et al.*, 2018; Hale, *et al.*, 2018; Hollywood, *et al.*, 2020; Mae, *et al.*, 2013; Przepiorski, *et al.*, 2018; Taguchi and Nishinakamura, 2017; Tanigawa, *et al.*, 2018). More recently, organoids have been successfully applied to understanding the pathogenesis of the infectious respiratory disease COVID-19, with SARS-CoV-2 viral infection and replication being achieved in a range of stem cell-derived tissues (Han, *et al.*, 2020; Marchiano, *et al.*, 2021; Mills, *et al.*, 2021; Sharma, *et al.*, 2020; Tiwari, *et al.*, 2021). Driven by the occurrence of AKI in COVID-19 patients (Huang, *et al.*, 2020; Kunutsor and Laukkanen, 2020; Yang, *et al.*, 2020; Zhou, *et al.*, 2020), a handful of studies have explored kidney organoids as a potential model of COVID-19 (Monteil, *et al.*, 2020; Wysocki, *et al.*, 2021). While it is still debated whether kidney damage results from direct viral infection or a combination of inflammatory responses and drug nephrotoxicity (reviewed in Motavalli, *et al.*, 2021), human PTs show high expression of the key SARS-CoV-2 receptor ACE2 (Kowalczuk, *et al.*, 2008; Hoffmann, *et al.*, 2020) and evidence of viral infection (Braun, *et al.*, 2020; Farkash, *et al.*, 2020; Kissling, *et al.*, 2020; Puelles, *et al.*, 2020; Su, *et al.*, 2020; Werion, *et al.*, 2020; Hanley, *et al.*, 2020). Given the high proportion of PT in enhanced organoids, we investigated their suitability as a model of SARS-CoV-2 infection and pathogenesis. Comprehensive analysis of scRNAseq data from >15,800 D13+14 organoid cells revealed expression levels and cellular localisation of a range of entry factors (receptors, proteases and binding proteins) previously implicated in SARS-CoV-2 infection (Amraei, *et al.*, 2021; Singh, *et al.*, 2020) (Figure 6A). While these entry factors were predominantly expressed within proximal tubule (clusters 1, 13 and 15), they were also observed in distal (clusters 9 and 17) nephron segments and endothelium (cluster 16) (Figure 6A). When comparing age- and line-matched organoids, all SARS-CoV-2 entry factors of the proximal and distal tubular segments showed increased expression levels and abundance in PT-enhanced organoids (Figure 6Bi-ii).

We next performed an in-depth investigation of the two most frequently reported viral entry factors in literature, *ACE2*/ACE2 and *TMPRSS2*/TMPRSS2 (Hoffmann, *et al.*, 2020). ScRNAseq and immunofluorescence demonstrated *ACE2*/ACE2 expression within the PT clusters of D13+14 organoids and localisation to the apical membrane of kidney organoid PTs, confirming previous reports *in vivo* and in kidney organoids (Kowalczuk, *et al.*, 2008; Camargo, *et al.*, 2009; Han, *et al.*, 2020; Monteil, *et al.*, 2020; Wysocki, *et al.*, 2021) (Figure 6AC). Apical ACE2 expression was also identified in epithelial cells lining the initial portion of Bowman's capsule transitioning from the S1 segment of the PT (Supplementary Figure 5A). Previous studies in mice have identified these transitionary cells as cuboidal and intermediate parietal epithelial cells (cuPECs and iPECs), making up the most proximal part of the proximal tubule prior to transitioning to flat PECs that line Bowmans's capsule (Kuppe, *et al.*, 2019; Wang, 2019). Accordingly, high *ACE2* gene expression correlated with a subset of cells co-expressing general PEC markers with a cuPEC/iPEC-specific profile (PAX8+, AKAP12+, PROM1-) (Supplementary Figure 5B). This region also partly coincided with the SLC34A1^{Hi}/HNF4A^{+}/SLC36A2^{+} population marking early (S1) PT cells (Lee, *et al.*, 2015; Broer, *et al.*, 2008) (Supplementary Figure 5C), which, along with LTL-positivity of the early Bowmans capsule epithelium (Supplementary Figure 5A), agreed with the known S1-PEC transitionary phenotype reported for cPECs and iPECs (Kuppe, *et al.*, 2019).

In contrast to a previous report in kidney organoids (Wysocki, *et al.*, 2021), *ACE2* and *TMPRSS2* were not co-expressed, instead being present within distinct nephron segments (proximal and distal, respectively), as has been observed in non-human primate kidney (Han, *et al.*, 2020) (Figure). *ACE2* was also absent from podocytes (cluster 12) (Figure 6A). To ensure this lack of co-expression was not the result of 'dropout' (failure to detect an expressed gene in single cell RNAseq), imputation was performed using Markov Affinity-based Graph Imputation of Cells (MAGIC; (van Dijk, *et al.*, 2018)). MAGIC-generated scatter plots confirmed a strong correlation (high R^2 linear correlation value) of *ACE2* and *TMPRSS2* with proximal tubule and distal tubule markers, respectively (Supplementary Figure 6A). This expression pattern was further supported by analyses of human fetal kidney, with expression of *ACE2* and *TMPRSS2*, along with additional SARS-CoV-2 entry factors, exhibiting a highly similar expression pattern to our extended kidney organoids (Supplementary Figure 6B). Using immunofluorescence, ACE2 protein was confirmed to reside on the apical membrane of organoid PTs, as observed in human kidney (Figure 6C) (Kowalczuk, *et al.*, 2008), in contrast

to the predominantly basolateral localisation of TMPRSS2 in distal tubule (Figure 6C and Supplementary Figure 6B). This would suggest viral entry is not reliant on TMPRSS2.

Having confirmed the expression of viral entry factors, PT-enhanced organoids were assessed for infectivity and viral replication following incubation in SARS-CoV-2 inoculum. Viral replication was detected in 3 independent replicate experiments as early as 2 days post-infection, with titres significantly increased compared to mock-infected organoids by day 6 post-infection ($P = 0.006$) (Figure 7A). Compared to standard organoids, PT-enhanced organoids showed higher levels of viral replication at 2 days post infection, reaching significance at 4 days post-infection ($P = 0.0253$), across independent experiments replicated using the same iPSC line and organoid conditions (Figure 7B). To determine the kidney cell types targeted by SARS-CoV-2, infected organoids were analysed via immunofluorescence for double stranded RNA (dsRNA) and nephron-specific markers 6 days post-infection (Figure 7C). DsRNA was observed predominantly in LTL-positive proximal tubules, as well as Bowman's capsule surrounding NPHS1-positive podocytes and portions of SLC12A1-positive Loops of Henle (Figure 7Ci-iii). No dsRNA was present in NPHS1-positive podocytes (Figure 7Fii), supporting ACE2 as the likely entry factor based on gene expression profiles (Figure 6A).

Discussion

The utility of human pluripotent stem cell-derived kidney organoids as models of kidney disease will rely upon nephron functional maturation. This is most critical for kidney organoid proximal tubules which, to date, have not shown significant evidence of functional solute transport. In this study, we show that changes to the initial maintenance of the nephron progenitor population, together with an inhibition of premature epithelialisation, results in improved proximal tubule maturation and unique alignment of nephrons along the proximodistal axis. This spatial arrangement is likely attributed to a WNT signalling gradient from the centre to the periphery of the organoid arising from the production of WNT inhibitors, including sFRP2, inducing a central ring of glomeruli from which sequential S1/S2 and S3 PT patterning occurs. This reinforces the requirement for a proximodistal gradient of WNT signalling for appropriate nephron patterning and segmentation.

While supporting a more proximal tubular phenotype, there was a bias away from distal tubule elements. Of importance, transcriptional profiling of D13 monolayers showed a high proportion of nephron progenitors with a significant increase in nephron progenitor gene expression (*SIX1, LYPD1*) and metanephric HOX ortholog expression (*HOX11A/C/D*) in comparison to all other comparable scRNASeq datasets. One of the unique features of this modified protocol includes the addition of nephron progenitor maintenance media, most importantly to prolong WNT agonism at low levels (C), suppress NOTCH signalling (D), and increase BMP7 activity (B). In agreement with this, mouse studies have shown a requirement for Notch to initiate nephron progenitor commitment (Boyle*, et al.*, 2011), with Notch signalling also required for nephron formation and Notch2 proposed to support proximal nephron patterning (Chung*, et al.*, 2017; Surendran*, et al.*, 2010). Low levels of canonical Wnt activity and Bmp/BMP signalling via MAPK and PI3K pathways have also been proposed to support nephron progenitor survival (Brown*, et al.*, 2015; Karner*, et al.*, 2011; Park*, et al.*, 2007; Blank*, et al.*, 2009; Lindstrom*, et al.*, 2015; Muthukrishnan*, et al.*, 2015). Despite containing both low CHIR and BMP7, the alternate nephron progenitor maintenance media NPSR was unable to support subsequent nephron formation in the resulting organoids. However, this may have been impacted by other variations in this media, such as the inclusion of BMP and TGFβ receptor inhibitors (dual inhibition of SMAD1/5/8 and SMAD2/3) (Li*, et al.*, 2016), which may maintain a less competent nephron progenitor population (Tanigawa*, et al.*, 2019).

PT-enhanced organoid formation had a less critical requirement for LIF (L) and Rho-kinase (ROCK) inhibition (Y). ROCK inhibition has previously been shown to prevent nephron patterning and elongation (Lindstrom, *et al.*, 2013). LIF has been suggested to induce mesenchymal-to-epithelial conversion (Barasch, *et al.*, 1999) but reduce the formation of developed nephrons (Bard and Ross, 1991). However, its effect may be somewhat complicated by concentration, with low LIF suggested to promote nephron progenitor expansion in culture via maintaining nuclear SIX2 and YAP, critical for self-renewal (Tanigawa, *et al.*, 2015). Timing of exposure remains an additional confounding factor, with the majority of growth factor requirement studies being performed in *ex vivo* cultured mouse or rat explants already possessing epithelializing structures within the mesenchyme.

It remains to be seen whether the outcome of this enhanced differentiation is a result of improved nephron progenitor expansion or sufficient time to form a more metanephric nephron progenitor population. Recent studies of the relative timing of PSC differentiation suggest that development and maturation *in vitro* is influenced by a predetermined species-specific biological clock. This has been elegantly demonstrated by Matsuda *et al* (2020), showing that the markedly different paces of differentiation exhibited by mouse and human PSCs can be attributed to biochemical rate variations that influence the segmentation clock (Matsuda, *et al.*, 2020). Indeed, brain organoids require months in culture to develop specific neural subtypes, akin to human gestation (Lancaster, *et al.*, 2013; Velasco, *et al.*, 2019). While our PT-enhanced kidney organoid protocol already shows considerable improvements in maturation after only 3 – 4 weeks, there is likely room for additional improvements in PT maturation that require optimisation of metabolic conditions beyond this time.

PT-enhanced kidney organoids do not simply show enhanced PT maturation, but also increased numbers of cells committed to a PT identity based on the HNF4A^{YFP} iPSC reporter line. Furthermore, this is the first report of functional proximal tubules within spatially aligned nephrons. We show that this is likely the response to a central zone of localised WNT antagonism likely emanating from the stroma. As such, the organoids appear to establish a sink and source of WNT activity along the length of the tubule which mimics the WNT signalling gradient required for appropriate proximodistal patterning (Lindstrom, *et al.*, 2015). The formation of a cartilage-forming stroma is problematic from the perspective of regenerating a transplantable tissue and has also been observed to form spontaneously after the transplantation of organoids generated using a number of distinct protocols (Bantounas, *et al.*, 2020; Nam, *et*

583 *al.*, 2019; van den Berg*, et al.*, 2018). It is possible that this cartilage arises from paraxial
584 mesoderm present within the culture, despite there being no increase in PARAXIS expression
585 compared to standard (D7) monolayer differentiations of the same age. Alternatively, this may
586 be a side-effect of the prolonged BMP signalling which could potentially be supressed through
587 SMAD1/5/8 inhibition. Nevertheless, the enhanced proximal tubular expansion, segmentation,
588 and maturation afforded by establishing a signalling gradient through localised WNT
589 antagonism represents a superior approach for the study of proximal tubule responses.

590 A clear example of the utility of such organoids for modelling infectious disease is illustrated
591 with the infection of PT-enhanced organoids with SARS-CoV-2. Our data shows an improved
592 capacity to infect PT-enhanced organoids with increased expression of previously identified
593 viral entry factors. In contrast to previous studies, we show no evidence for a dual requirement
594 for TMPRSS2 and ACE2 for PT infection, given the separation in both cell type distribution
595 and apical-basal protein insertion between these two proteins. However, analysis of dsRNA
596 staining suggests that SARS-CoV-2 can enter distal portions of the nephron, suggesting
597 multiple entry pathways are at play. Establishing such entry mechanisms are of keen interest
598 to the renal community. ACE2 binding by SARS-CoV-2 results in a downregulation of the
599 renin angiotensin system (RAS) by reducing the conversion of angiotensin I (Ang I) and
600 angiotensin II (Ang II) to phosphorylated products angiotensin 1-9 angiotensin 1-7,
601 respectively (reviewed in Silhol*, et al.*, 2020). This leads to higher plasma concentrations of
602 Ang I and subsequently Ang II (via angiotensin converting enzyme; ACE), increased binding
603 of Ang II to its receptor (AT1R), and activation of systemic responses such as vasoconstriction,
604 aldosterone secretion stimulation, hypokalemia, inflammation, and fibrosis (Silhol*, et al.*, 2020;
605 Reddy*, et al.*, 2019). As such, the renal community has been interested to know whether renal
606 failure patients on ACE inhibitors (control Ang I/II conversion) are at greater or less risk of
607 renal damage in response to COVID-19 (Diaz, 2020; Esler and Esler, 2020; Fang*, et al.*, 2020;
608 Hippisley-Cox*, et al.*, 2020; Li*, et al.*, 2021; Vaduganathan*, et al.*, 2020).

609 The PT-enhanced organoid model provides an opportunity to evaluate the impact of viral entry,
610 ACE2 expression level, and the response of cells to ACE inhibition during infection. However,
611 this model may also provide a superior testbed for screening of different SARS-CoV-2 variants
612 in addition to other viral infections of the kidney such as BK virus, a major challenge in
613 immunosuppressed kidney transplant recipients (Herrera*, et al.*, 2021). While previous adult
614 kidney tubuloids have been infected with BK virus (Schutgens*, et al.*, 2019), the definitive

identity of these tubules is not clear. As such, the maturity and distinct S1/S2/S3 segmentation within PT-enhanced organoids, along with evidence for distal nephron, offer a unique opportunity to study viral mechanisms. These advantages, combined with the suitability of PT-enhanced kidney organoids to elicit the appropriate response to drug-induced injury, makes this an ideal platform for disease research applications while providing insight into improving our control over the spatial organisation of bioengineered tissue.

Methods

iPSC lines and maintenance

iPSC lines used in this study include CRL1502.C32 (Takasato, *et al.*, 2015; Briggs, *et al.*, 2013) CRL-2429/SIX2$^{Cre/Cre}$:GAPDH^{dual} (Howden, *et al.*, 2019), PCS-201-010/HNF4A^{YFP} (Vanslambrouck, *et al.*, 2019), and PB010/MCRIi010-A (Vlahos, *et al.*, 2019). All iPSC lines were maintained and expanded at 37˚C, 5% CO_2 and 5% O_2 in Essential 8 medium (Thermo Fisher Scientific, Waltham, MA) on Matrigel- (BioStrategy, Victoria, Australia) coated plates with daily media changes and passaged every 2 – 3 days with EDTA in 1X PBS as described previously (Chen, *et al.*, 2011).

Directed differentiation and kidney organoid generation

For standard organoid production, differentiation of iPSC lines and organoid culture was performed as described previously (Howden, *et al.*, 2019), with minor variations in the concentration of Laminin-521 (BioLamina, Sundbyberg, Sweden) used to coat 12-well plates, initial iPSC seeding density within 12-well plates, and CHIR99021 (R&D Systems) concentration and duration of exposure according to the iPSC line used (CRL1502.C32, CRL-2429/SIX2$^{Cre/Cre}$:GAPDH^{dual} and PB010/MCRIi010-A were seeded at 25,000 cells/well and exposed to 6µM CHIR for 5 days; PCS-201-010/HNF4A^{YFP} was seeded at 40,000 cells/well and exposed to 6µM CHIR for 4 days; CRL1502.C32, CRL-2429/SIX2$^{Cre/Cre}$:GAPDH^{dual} were seeded with 20µL/mL Laminin-521; PB010/MCRIi010-A and PCS-201-010/HNF4A^{YFP} were seeded with 40µL/mL Laminin-521). Standard bioprinted patch organoids were generated as described previously (Lawlor, *et al.*, 2021).

For PT-enhanced organoids, Matrigel concentrations and iPSC seeding density for differentiation in 12-well plates were as stated for standard organoids above. iPSCs were then subjected to prolonged monolayer differentiation in 6µM CHIR for 5 days, followed by 200ng/mL FGF9 (R&D Systems) and 1µg/mL heparin (Sigma Aldrich) until day 8, refreshing the media every second day. At day 8, the monolayer was exposed to 1mL/well nephron progenitor maintenance media, NPSR or CDBLY (Li, *et al.*, 2016; Tanigawa, *et al.*, 2016), refreshing these media daily. Final PT-enhanced organoid conditions utlised CDBLY2,

containing 2X concentration of BMP7. Organoids were generated and cultured as described previously (Takasato, *et al.*, 2016).

Immunofluorescence and confocal microscopy

For immunofluorescence, organoids were prepared and stained as previously described (Vanslambrouck, *et al.*, 2019) using the antibodies detailed in Table 1, diluted in 0.1% TX-100/PBS. Imaging was performed on the ZEISS LSM 780 confocal microscope (Carl Zeiss, Oberkochen, Germany) with acquisition and processing performed using ZEISS ZEN Black software (Zeiss Microscopy, Thornwood, NY) and Fiji ImageJ (Schindelin, *et al.*, 2012).

Flow cytometry

Flow cytometry of reporter line-derived organoids using endogenous fluorescence was performed and analysed as described previously (Vanslambrouck, *et al.*, 2019). To determine the contribution of SIX2-mCherry + cells to EPCAM+ populations in organoids derived from the $SIX2^{Cre}$ lineage tracing iPSC line, dissociated and strained cells were stained using directly conjugated anti-EPCAM Alexa Fluor-647 antibody (see Table 1) diluted 1:100 in 100 µL of FACS wash (1% fetal calf serum [FCS] in PBS) for every 5 $x10^5$ cells. Following 30 minutes incubation on ice, cells were washed 3 times in 2mL FACS wash via centrifugation prior to flow cytometry.

Histology

For Alcian Blue detection of cartilage, organoids were fixed in 4% PFA as described above and processed for routine paraffin embedding using the Excelsior AS Tissue Processor (rapid biopsy setting; Thermo Fisher Scientific). Samples were embedded in wax and 5µm sections cut using a Waterfall HM325 microtome (Thermo Fisher Scientific). Sections were dewaxed, hydrated through graded alcohols to running water, then covered with Alcian Blue Solution (1% Alcian blue in 3% acetic acid, pH 2.5). After 10 minutes, sections were washed in tap water for 2 minutes and counterstained for 7 minutes in Nuclear Fast Red stain (0.1% Nuclear Fast Red [Sigma Aldrich, St Louise, MO] and 5% ammonium potassium sulfate in water). Following staining, sections were dehydrated in graded alcohols, cleared in Safsolvent (Bacto

Laboratories, NSW, Australia), and coverslipped. Images were acquired on a Zeiss Axio Imager A2 with Zeiss Zen software (Zeiss Microscopy, Thornwood, NY).

Real-time quantitative reverse transcription PCR (qRT-PCR)

RNA extraction, cDNA synthesis and quantitative RT-PCR (qRT-PCR) were performed using the Bioline Isolate II Mini/Micro RNA Extraction Kit, SensiFAST cDNA Synthesis Kit and the SensiFAST SYBR Lo-ROX Kit (Bioline, NSW, Australia), respectively, as per manufacturer's instructions. Each qRT-PCR reaction was performed in triplicate using the primer pairs detailed in Table 2. Data were graphed and analysed in Prism 8 (GraphPad).

Single cell RNA sequencing (scRNAseq) and dataset generation

The D13+12 dataset was generated using the CRL-2429/SIX2$^{Cre/Cre}$:GAPDH^{dual} iPSC line. The D13 and D13+14 organoids were generated using the CRL1502.C32 with four replicates per time point, where each replicate was derived from an independent well. Cells were dissociated following previously published methods (Lawlor*, et al.*, 2021). For the D13 and D13+14 samples, replicates were multiplexed following the method of Soeckius et al. (Stoeckius*, et al.*, 2018). Cells were stained for 20 minutes on ice with 1µg of BioLegend TotalSeq-A anti-human hashtag oligo antibody (BioLegend TotalSeq-A0251 to A0258). Cells were washed 3 times then pooled at equal ratios for sequencing. A single library was generated for each suspension/condition, composed of equally sized pools of each replicate (Set 1 – 4). Libraries were generated following the standard 10x Chromium Next GEM Single Cell 3′ Reagent Kits v3.1 protocol except that 'superloading' of the 10x device was performed with ~30k cells. Hash tag oligo (HTO) libraries were generated following the BioLegend manufacturer protocol. Sequencing was performed using an Illumina Novoseq.

10x mRNA libraries were demultiplexed using CellRanger (3.1.0) to generate matrices of UMI counts per cell. HTO libraries were demultiplexed using Cite-seq-count (1.4.3) to generate matrices of HTO counts per cell barcode. All data were loaded into Seurat (3.1.4) and HTO libraries were matched to mRNA libraries. Seurat was used to normalise HTO counts and determine cut-offs to assign HTO identity per cell using the *HTODemux* function with the positive.quantile parameter set at 0.99. HTO doublet and unassigned cells were removed, as were cells with mitochondrial content greater than 35% accounting for the increased metabolic

activity of renal epithelium (Ransick, *et al.*, 2019), number of genes per cell greater than 500 and the number of UMIs less than 100000, to obtain filtered datasets (D13 replicates: 3694 cells [A0251], 3545 cells [A0252], 3785 cells [A0253], 3641 cells [A0254]; D13+14 replicates: 3415 cells [A0255], 2350 cells [A0256], 2904 cells [A0257], 2578 cells [A0258]). The combined datasets contained a median of 3915 genes expressed per cell, with a median of 16352 UMI counts per cell.

Analysis of scRNAseq datasets

Data was normalised using the SCTransform method (Hafemeister and Satija, 2019) including the regression of cell cycle scores. A 30 component Principal Component Analysis (PCA) was performed, followed by Uniform Manifold Approximation and Projection (UMAP) using these PCA components. Seurat's graph-based clustering approach was used to identify, with resolutions of 0.7 (D13) and 0.5 (D13+14) chosen for downstream analysis. Marker analysis was performed using the Seurat *FindMarkers* function, using student's t-test, limited to positive markers (i.e. increased expression within a cluster) above 0.25 log fold-change expressed in at least 10% of cells within a cluster. Marker lists were exported and cluster identities were determined by comparison with published human single cell data (Howden, *et al.*, 2019) or Gene ontology analysis using ToppFun (https://toppgene.cchmc.org/enrichment.jsp). The proximal tubule cluster was isolated and reanalysed as above to further investigate any subpopulations.

The D13+12 dataset was integrated with an age- and line-matched published dataset (Howden, *et al.*, 2019) using the anchor-based method within Seurat (Butler, *et al.*, 2018; Stuart, *et al.*, 2019). This integrated dataset was analysed as above, isolating the proximal tubule cluster and comparing gene expression of cells from both samples within this population.

For DevKidCC analyses, the D13 and D13p14 samples were analysed using DevKidCC (v.0.2.2); a hierarchical set of machine-learning binary classifiers trained on a human fetal kidney reference dataset. The classified dataset was then compared to relevant existing single cell organoid datasets using the *DotPlotCompare* function.

Agarose bead-mediated morphogen signalling assay

Bioprinted patch organoids were generated and cultured as described previously prior to the addition of morphogen-soaked beads at D7+5 (Lawlor, *et al.*, 2021). The day before bead addition, 100µL of Affi-Gel Blue Gel 100 – 200 mesh crosslinked agarose beads (Bio-Rad Laboratories, Hercules, CA), were washed 3 times in PBS via centrifugation. Washed beads were resuspended in 100µL of PBS (control) or 10µM IWR-1 (stock reconstituted according to manufacturer's instructions; Sigma Aldrich) and incubated for 1 hour at room temperature prior to overnight storage at 4ºC. On day 7+5, suspensions were agitated to resuspend beads and 0.3 µL was added to the centre of each patch organoid with the aid of a P2 pipette and dissecting microscope (Leica Microsystems, Wetzlar, Germany). Organoid media (TeSR-E6 [STEMCELL Technologies, Vancouver, Canada]) was refreshed every second day prior to harvest at D7+9 for immunofluorescence.

Cisplatin toxicity assay

D13+14 PT-enhanced organoids were exposed through the basolateral compartment of the Transwell tissue culture plate (Corning Incorporated, Corning, NY) to 1mL per well of 20 µM Cisplatin (Accord Healthcare, Durham, NC), or an equivalent volume of PBS, in TeSR-E6 for 24 hours (37˚C, 5% CO_2 and 5% O_2). Following incubation, organoids within Transwells were washed with PBS and harvested for flow cytometry as described above.

Fluorescent substrate uptake assays

For albumin uptake assays, D13+14 PT-enhanced organoids (triplicate wells per condition) were incubated in TRITC albumin (1:1000, Sigma Aldrich) and anti-MEGALIN/LRP2 (1:500, pre-incubated with an alpaca Nano-secondary Alexa Fluor 647 secondary antibody diluted in TeSR-E6 culture media via the basolateral compartment of Transwell tissue culture plates and incubated overnight (37˚C, 5% CO_2 and 5% O_2). Control organoids were incubated in secondary antibody alone. After incubation, plates containing organoids were washed in at least 3 changes of Hanks' Balanced Salt Solution (HBSS; Thermo Fisher Scientific) for 30 minutes and live-imaged immediately using a ZEISS LSM 780 confocal microscope. For organic cation transport assays, D13+14 PT-enhanced organoids (triplicate wells per condition) were incubated in 4',6-diamindino-2-phenylindole substrate (DAPI; 1:1000 [Thermo Fisher Scientific]) with 1:500 DRAQ7 dead cell label (Thermo Fisher Scientific]) diluted in TeSR-E6 for 1 hour (37˚C, 5% CO_2 and 5% O_2). Control organoids were pre-incubated for 15 minutes

767 in 100 µM Cimetidine inhibitor (Sigma Aldrich) prior to incubation for 1 hour in TeSR-E6
768 containing both inhibitor, substrate, and dead cell label (1:1000 DAPI, 1:500 DRAQ7, 100 µM
769 Cimetidine). Following incubation, substrate and substrate + inhibitor solutions were replaced
770 with HBSS and live-imaged immediately using a ZEISS LSM 780 confocal microscope.

771 ***Viral infection assays***

772 Standard and PT-enhanced organoids grown on Transwells were infected with 10^4 tissue-
773 culture infectious dose 50 ($TCID_{50}$) of SARS-CoV-2 (Australia/VIC01/2020) in TeSR-E6
774 media, added either above or below the Transwell, for 1 – 3 hours (37˚C and 5% CO_2).
775 Following incubation, the viral inoculum was removed and replaced with 1mL of plain TeSR-
776 E6 medium beneath the Transwell as for typical organoid culture (Takasato*, et al.*, 2016).
777 Culture medium was collected on days 0, 2, 4, and 6 post-infection for viral titer quantification
778 and replaced with fresh medium. Median $TCID_{50}$ in supernatants were determined, as detailed
779 below, by 10- fold serial dilution in Vero cells and calculated using the Reed and Muench
780 method. Organoids were harvested at 6 days post-infection and and fixed with 4% PFA fixation
781 for immunofluorescence.

782 ***Infectious virus titration ($TCID_{50}$)***

783 Viral titrations were performed on confluent monolayers of Vero cells in 96-well plates. Wells
784 were washed with plain minimum essential media (MEM) and replaced with 180µl of infection
785 media (MEM, 50U/ml Penicillin, 50µg/ml Streptomycin, 2mM GlutaMax, 15mM HEPES and
786 1µg/ml TPCK-treated Trypsin). 20µl of the samples to be titred were added to four wells and
787 10-fold serial dilutions were made. Plates were incubated at 37˚C and 5% CO_2. Four days post-
788 infection, SARS-CoV-2-induced cytopathic effect was assessed by microscopy.

789

790

791

792 **Tables**

793 **Table 1.** Antibodies used in immunofluorescence studies.

Specificity	Host species	Dilution range	Manufacturer and identifier
ACE2	Rabbit	1:300	Abcam (ab15348)
CUBILIN	Goat	1:300	Santa Cruz Biotechnology (sc-20607)
dsRNA	Mouse	1:300	Absolute Antibody (Ab01299-2.0)
ECADHERIN	Mouse	1:300	BD Biosciences (610181)
EpCAM (Alexa488 or Alexa647 conjugate)	Mouse	1:300	BioLegend (324210 and 324212)
GATA3	Goat or rabbit	1:300	R&D Systems (AF2605) and Cell Signalling Technology (95852S)
HNF4A	Mouse	1:300	Life Technologies (MA1-199)
KIM-1	Goat	1:300	R&D Systems (AF1750)
mCherry (RFP)	Rabbit	1:300 – 1:400	MBL Medical & Biological Laboratories Co. Ltd. (PM005)
MEGALIN	Rabbit	1:300	Sapphire Bioscience (NBP2-39033)
NEPHRIN	Sheep	1:300	R&D Systems (AF4269)
Proximal tubule brush border membrane	*Lotus tetragonobulus* lectin (LTL)	1:300 – 1:500	Vector Laboratories (B-1325)
TMPRSS2	Mouse	1:300	Merck (MABF2158-25UG)
SLC6A19	Chicken	1:100 – 1:200	Aves Laboratories (custom antibody)
SLC12A1	Rabbit	1:300 – 1:400	Proteintech (18970-1-AP)

794

795 **Table 2.** Forward and reverse primers used for qRT-PCR.

Gene	Forward primer (5'-3')	Reverse primer (5'-3')
DAPL1	CTCGGAAAGGGGGACATCCT	AGTTGAGCTTCTCCAGTGCG

GAPDH	CTCTCTGCTCCTCCTGTTCGA	TGAGCGATGTGGCTCGGCT
GATA3	GCCCCTCATTAAGCCCAAG	TTGTGGTGGTCTGACAGTTCG
HAVCR1	GTTCCTCCAATGCCTTTGCC	CGGTGTCATTCCCATCTGTTG
HNF4A	ACCCTCGTCGACATGGACA	GCCTTCTGATGGGGACGTG
HOXD11	GCCAGTGTGCTGTCGTTCCC	CTTCCTACAGACCCCGCCGT
LHX1	CGTCATTCAGGTCTGGTTCC	CCCGTAGTACTCGCTCTGGT
PARAXIS	GGGGGTGGCCGTCGT	CAGGCTGAATGGATCCTCAC
SIX1	AAAGGGAAGGAGAACAAGGATAG	GGAGCCTACATGATTACTGGG
SIX2	TCCTGGTCCCTCCGTATGTA	TAGGGGCAGATAGACCACCA
TMEM-100	CAGGCGTTGCTGTTTCTTGT	CAGGGTGAAAGCTCGGAGAG
WNT4	AACTGCTCCACACTCGACTC	TGACCACTGGAAGCCCTGT

Acknowledgements

We thank Maelle Le Moing and the Murdoch Children's Research Institute Translational Genomics Unit for 10x single cell and hash-tag oligo library preparation and sequencing, and bulk-RNAseq sequencing; Dr Matthew Burton and the Murdoch Children's Research Institute Microscopy Core; Professor John Rasko and Dr Charles Bailey for providing the SLC6A19 antibody.

Author Contributions

JMV, MHL, and KS contributed to experimental design and planning. JMV, KST, EG, RR, JN, MS, and SEH performed experiments and developed reagents and methods. SBW and JMV performed bioinformatics analyses. JMV, MHL, and SBW contributed to manuscript preparation. JMV and MHL wrote the manuscript.

Data availability

All transcriptional profiling datasets have been submitted to GEO (GSE184928). These including single cell RNAseq from D13 monolayer differentiation, D13+14 PT-enhanced kidney organoids, and D13+12 PT-enhanced kidney organoid.

Competing interests

The authors declare they have no competing interests.

References

1 Collaboration, G. B. D. C. K. D. Global, regional, and national burden of chronic kidney disease, 1990-2017: a systematic analysis for the Global Burden of Disease Study 2017. *Lancet* **395**, 709-733, doi:10.1016/S0140-6736(20)30045-3 (2020).

2 Kirita, Y., Wu, H., Uchimura, K., Wilson, P. C. & Humphreys, B. D. Cell profiling of mouse acute kidney injury reveals conserved cellular responses to injury. *Proc Natl Acad Sci U S A* **117**, 15874-15883, doi:10.1073/pnas.2005477117 (2020).

3 Zhuo, J. L. & Li, X. C. Proximal nephron. *Compr Physiol* **3**, 1079-1123, doi:10.1002/cphy.c110061 (2013).

4 Freedman, B. S., Brooks, C. R., Lam, A. Q., Fu, H., Morizane, R., Agrawal, V., Saad, A. F., Li, M. K., Hughes, M. R., Werff, R. V., Peters, D. T., Lu, J., Baccei, A., Siedlecki, A. M., Valerius, M. T., Musunuru, K., McNagny, K. M., Steinman, T. I., Zhou, J., Lerou, P. H. & Bonventre, J. V. Modelling kidney disease with CRISPR-mutant kidney organoids derived from human pluripotent epiblast spheroids. *Nature communications* **6**, 8715, doi:10.1038/ncomms9715 (2015).

5 Morizane, R., Lam, A. Q., Freedman, B. S., Kishi, S., Valerius, M. T. & Bonventre, J. V. Nephron organoids derived from human pluripotent stem cells model kidney development and injury. *Nature biotechnology* **33**, 1193-1200, doi:10.1038/nbt.3392 (2015).

6 Taguchi, A., Kaku, Y., Ohmori, T., Sharmin, S., Ogawa, M., Sasaki, H. & Nishinakamura, R. Redefining the in vivo origin of metanephric nephron progenitors enables generation of complex kidney structures from pluripotent stem cells. *Cell Stem Cell* **14**, 53-67, doi:10.1016/j.stem.2013.11.010 (2014).

7 Toyohara, T., Mae, S., Sueta, S., Inoue, T., Yamagishi, Y., Kawamoto, T., Kasahara, T., Hoshina, A., Toyoda, T., Tanaka, H., Araoka, T., Sato-Otsubo, A., Takahashi, K., Sato, Y., Yamaji, N., Ogawa, S., Yamanaka, S. & Osafune, K. Cell Therapy Using Human Induced Pluripotent Stem Cell-Derived Renal Progenitors Ameliorates Acute Kidney Injury in Mice. *Stem cells translational medicine* **4**, 980-992, doi:10.5966/sctm.2014-0219 (2015).

8 Combes, A. N., Phipson, B., Lawlor, K. T., Dorison, A., Patrick, R., Zappia, L., Harvey, R. P., Oshlack, A. & Little, M. H. Single cell analysis of the developing mouse kidney provides deeper insight into marker gene expression and ligand-receptor crosstalk. *Development* **146**, doi:10.1242/dev.178673 (2019).

9 Howden, S. E., Wilson, S. B., Groenewegen, E., Starks, L., Forbes, T. A., Tan, K. S., Vanslambrouck, J. M., Holloway, E. M., Chen, Y. H., Jain, S., Spence, J. R. & Little, M. H. Plasticity of distal nephron epithelia from human kidney organoids enables the induction of ureteric tip and stalk. *Cell Stem Cell* **28**, 671-684 e676, doi:10.1016/j.stem.2020.12.001 (2021).

10 Subramanian, A., Sidhom, E. H., Emani, M., Vernon, K., Sahakian, N., Zhou, Y., Kost-Alimova, M., Slyper, M., Waldman, J., Dionne, D., Nguyen, L. T., Weins, A., Marshall, J. L., Rosenblatt-Rosen, O., Regev, A. & Greka, A. Single cell census of human kidney organoids shows reproducibility and diminished off-target cells after transplantation. *Nature communications* **10**, 5462, doi:10.1038/s41467-019-13382-0 (2019).

11 Wu, H., Uchimura, K., Donnelly, E. L., Kirita, Y., Morris, S. A. & Humphreys, B. D. Comparative Analysis and Refinement of Human PSC-Derived Kidney Organoid Differentiation with Single-Cell Transcriptomics. *Cell Stem Cell* **23**, 869-881 e868, doi:10.1016/j.stem.2018.10.010 (2018).

12 Takasato, M., Er, P. X., Chiu, H. S., Maier, B., Baillie, G. J., Ferguson, C., Parton, R. G., Wolvetang, E. J., Roost, M. S., Chuva de Sousa Lopes, S. M. & Little, M. H. Kidney organoids from human iPS cells contain multiple lineages and model human nephrogenesis. *Nature* **526**, 564-568, doi:10.1038/nature15695 (2015).

13 Takasato, M., Er, P. X., Chiu, H. S. & Little, M. H. Generation of kidney organoids from human pluripotent stem cells. *Nature protocols* **11**, 1681-1692, doi:10.1038/nprot.2016.098 (2016).

14 Marable, S. S., Chung, E. & Park, J. S. Hnf4a Is Required for the Development of Cdh6-Expressing Progenitors into Proximal Tubules in the Mouse Kidney. *J Am Soc Nephrol* **31**, 2543-2558, doi:10.1681/ASN.2020020184 (2020).

15 Wilson, S. B., Howden, S. E., Vanslambrouck, J. M., Dorison, A., Alquicira-Hernandez, J., Powell, J. E. & Little, M. H. DevKidCC allows for robust classification and direct comparisons of kidney organoid datasets. *bioRxiv*, doi:10.1101/2021.01.20.427346 (2021).

16 Dressler, G. R. Advances in early kidney specification, development and patterning. *Development* **136**, 3863-3874, doi:10.1242/dev.034876 (2009).

17 de Bakker, B. S., van den Hoff, M. J. B., Vize, P. D. & Oostra, R. J. The Pronephros; a Fresh Perspective. *Integr Comp Biol* **59**, 29-47, doi:10.1093/icb/icz001 (2019).

18 Kobayashi, A., Valerius, M. T., Mugford, J. W., Carroll, T. J., Self, M., Oliver, G. & McMahon, A. P. Six2 defines and regulates a multipotent self-renewing nephron progenitor population throughout mammalian kidney development. *Cell Stem Cell* **3**, 169-181, doi:10.1016/j.stem.2008.05.020 (2008).

19 Lindstrom, N. O., McMahon, J. A., Guo, J., Tran, T., Guo, Q., Rutledge, E., Parvez, R. K., Saribekyan, G., Schuler, R. E., Liao, C., Kim, A. D., Abdelhalim, A., Ruffins, S. W., Thornton, M. E., Baskin, L., Grubbs, B., Kesselman, C. & McMahon, A. P. Conserved and Divergent Features of Human and Mouse Kidney Organogenesis. *J Am Soc Nephrol* **29**, 785-805, doi:10.1681/ASN.2017080887 (2018).

20 Georgas, K. M., Chiu, H. S., Lesieur, E., Rumballe, B. A. & Little, M. H. Expression of metanephric nephron-patterning genes in differentiating mesonephric tubules. *Dev Dyn* **240**, 1600-1612, doi:10.1002/dvdy.22640 (2011).

21 Mugford, J. W., Sipila, P., Kobayashi, A., Behringer, R. R. & McMahon, A. P. Hoxd11 specifies a program of metanephric kidney development within the intermediate mesoderm of the mouse embryo. *Dev Biol* **319**, 396-405, doi:10.1016/j.ydbio.2008.03.044 (2008).

22 Tiedemann, K., Welling, L. W. & Basto, P. Structural and functional comparison of mesonephric and metanephric proximal tubules. *Pediatr Nephrol* **1**, 297-305, doi:10.1007/BF00849227 (1987).

898 23 Howden, S. E., Vanslambrouck, J. M., Wilson, S. B., Tan, K. S. & Little, M. H. Reporter-based fate mapping in human kidney organoids confirms nephron lineage relationships and reveals synchronous nephron formation. *EMBO Rep*, doi:10.15252/embr.201847483 (2019).

902 24 Vanslambrouck, J. M., Wilson, S. B., Tan, K. S., Soo, J. Y., Scurr, M., Spijker, H. S., Starks, L. T., Neilson, A., Cui, X., Jain, S., Little, M. H. & Howden, S. E. A Toolbox to Characterize Human Induced Pluripotent Stem Cell-Derived Kidney Cell Types and Organoids. *J Am Soc Nephrol* **30**, 1811-1823, doi:10.1681/ASN.2019030303 (2019).

906 25 Little, M. H. & Combes, A. N. Kidney organoids: accurate models or fortunate accidents. *Genes Dev* **33**, 1319-1345, doi:10.1101/gad.329573.119 (2019).

908 26 Tsujimoto, H., Kasahara, T., Sueta, S. I., Araoka, T., Sakamoto, S., Okada, C., Mae, S. I., Nakajima, T., Okamoto, N., Taura, D., Nasu, M., Shimizu, T., Ryosaka, M., Li, Z., Sone, M., Ikeya, M., Watanabe, A. & Osafune, K. A Modular Differentiation System Maps Multiple Human Kidney Lineages from Pluripotent Stem Cells. *Cell reports* **31**, 107476, doi:10.1016/j.celrep.2020.03.040 (2020).

913 27 Brown, A. C., Muthukrishnan, S. D. & Oxburgh, L. A synthetic niche for nephron progenitor cells. *Developmental cell* **34**, 229-241, doi:10.1016/j.devcel.2015.06.021 (2015).

916 28 Li, Z., Araoka, T., Wu, J., Liao, H. K., Li, M., Lazo, M., Zhou, B., Sui, Y., Wu, M. Z., Tamura, I., Xia, Y., Beyret, E., Matsusaka, T., Pastan, I., Rodriguez Esteban, C., Guillen, I., Guillen, P., Campistol, J. M. & Izpisua Belmonte, J. C. 3D Culture Supports Long-Term Expansion of Mouse and Human Nephrogenic Progenitors. *Cell Stem Cell* **19**, 516-529, doi:10.1016/j.stem.2016.07.016 (2016).

921 29 Tanigawa, S., Sharma, N., Hall, M. D., Nishinakamura, R. & Perantoni, A. O. Preferential Propagation of Competent SIX2+ Nephronic Progenitors by LIF/ROCKi Treatment of the Metanephric Mesenchyme. *Stem Cell Reports* **5**, 435-447, doi:10.1016/j.stemcr.2015.07.015 (2015).

925 30 Tanigawa, S., Taguchi, A., Sharma, N., Perantoni, A. O. & Nishinakamura, R. Selective In Vitro Propagation of Nephron Progenitors Derived from Embryos and Pluripotent Stem Cells. *Cell reports* **15**, 801 - 813, doi:10.1016/j.celrep.2016.03.076 (2016).

928 31 Lindstrom, N. O., Lawrence, M. L., Burn, S. F., Johansson, J. A., Bakker, E. R.,
929 Ridgway, R. A., Chang, C. H., Karolak, M. J., Oxburgh, L., Headon, D. J., Sansom, O.
930 J., Smits, R., Davies, J. A. & Hohenstein, P. Integrated beta-catenin, BMP, PTEN, and
931 Notch signalling patterns the nephron. *Elife* **3**, e04000, doi:10.7554/eLife.04000
932 (2015).

933 32 Takasato, M., Er, P. X., Becroft, M., Vanslambrouck, J. M., Stanley, E. G., Elefanty,
934 A. G. & Little, M. H. Directing human embryonic stem cell differentiation towards a
935 renal lineage generates a self-organizing kidney. *Nature cell biology* **16**, 118-126,
936 doi:10.1038/ncb2894 (2014).

937 33 Hochane, M., van den Berg, P. R., Fan, X., Berenger-Currias, N., Adegeest, E.,
938 Bialecka, M., Nieveen, M., Menschaart, M., Chuva de Sousa Lopes, S. M. & Semrau,
939 S. Single-cell transcriptomics reveals gene expression dynamics of human fetal kidney
940 development. *PLoS Biol* **17**, e3000152, doi:10.1371/journal.pbio.3000152 (2019).

941 34 Lindstrom, N. O., De Sena Brandine, G., Tran, T., Ransick, A., Suh, G., Guo, J., Kim,
942 A. D., Parvez, R. K., Ruffins, S. W., Rutledge, E. A., Thornton, M. E., Grubbs, B.,
943 McMahon, J. A., Smith, A. D. & McMahon, A. P. Progressive Recruitment of
944 Mesenchymal Progenitors Reveals a Time-Dependent Process of Cell Fate Acquisition
945 in Mouse and Human Nephrogenesis. *Developmental cell* **45**, 651-660 e654,
946 doi:10.1016/j.devcel.2018.05.010 (2018).

947 35 Lindstrom, N. O., Guo, J., Kim, A. D., Tran, T., Guo, Q., De Sena Brandine, G.,
948 Ransick, A., Parvez, R. K., Thornton, M. E., Basking, L., Grubbs, B., McMahon, J. A.,
949 Smith, A. D. & McMahon, A. P. Conserved and Divergent Features of Mesenchymal
950 Progenitor Cell Types within the Cortical Nephrogenic Niche of the Human and Mouse
951 Kidney. *J Am Soc Nephrol* **29**, 806-824, doi:10.1681/ASN.2017080890 (2018).

952 36 Lindstrom, N. O., Tran, T., Guo, J., Rutledge, E., Parvez, R. K., Thornton, M. E.,
953 Grubbs, B., McMahon, J. A. & McMahon, A. P. Conserved and Divergent Molecular
954 and Anatomic Features of Human and Mouse Nephron Patterning. *J Am Soc Nephrol*
955 **29**, 825-840, doi:10.1681/ASN.2017091036 (2018).

956 37 Low, J. H., Li, P., Chew, E. G. Y., Zhou, B., Suzuki, K., Zhang, T., Lian, M. M., Liu,
957 M., Aizawa, E., Rodriguez Esteban, C., Yong, K. S. M., Chen, Q., Campistol, J. M.,
958 Fang, M., Khor, C. C., Foo, J. N., Izpisua Belmonte, J. C. & Xia, Y. Generation of

Human PSC-Derived Kidney Organoids with Patterned Nephron Segments and a De Novo Vascular Network. *Cell Stem Cell* **25**, 373-387 e379, doi:10.1016/j.stem.2019.06.009 (2019).

38 Tran, T., Lindstrom, N. O., Ransick, A., De Sena Brandine, G., Guo, Q., Kim, A. D., Der, B., Peti-Peterdi, J., Smith, A. D., Thornton, M., Grubbs, B., McMahon, J. A. & McMahon, A. P. In Vivo Developmental Trajectories of Human Podocyte Inform In Vitro Differentiation of Pluripotent Stem Cell-Derived Podocytes. *Developmental cell* **50**, 102-116 e106, doi:10.1016/j.devcel.2019.06.001 (2019).

39 Holloway, E. M., Wu, J. H., Czerwinski, M., Sweet, C. W., Wu, A., Tsai, Y. H., Huang, S., Stoddard, A. E., Capeling, M. M., Glass, I. & Spence, J. R. Differentiation of Human Intestinal Organoids with Endogenous Vascular Endothelial Cells. *Developmental cell* **54**, 516-528 e517, doi:10.1016/j.devcel.2020.07.023 (2020).

40 Czerniecki, S. M., Cruz, N. M., Harder, J. L., Menon, R., Annis, J., Otto, E. A., Gulieva, R. E., Islas, L. V., Kim, Y. K., Tran, L. M., Martins, T. J., Pippin, J. W., Fu, H., Kretzler, M., Shankland, S. J., Himmelfarb, J., Moon, R. T., Paragas, N. & Freedman, B. S. High-Throughput Screening Enhances Kidney Organoid Differentiation from Human Pluripotent Stem Cells and Enables Automated Multidimensional Phenotyping. *Cell Stem Cell* **22**, 929-940 e924, doi:10.1016/j.stem.2018.04.022 (2018).

41 Harder, J. L., Menon, R., Otto, E. A., Zhou, J., Eddy, S., Wys, N. L., O'Connor, C., Luo, J., Nair, V., Cebrian, C., Spence, J. R., Bitzer, M., Troyanskaya, O. G., Hodgin, J. B., Wiggins, R. C., Freedman, B. S., Kretzler, M., European Renal c, D. N. A. B. & Nephrotic Syndrome Study, N. Organoid single cell profiling identifies a transcriptional signature of glomerular disease. *JCI Insight* **4**, doi:10.1172/jci.insight.122697 (2019).

42 Kumar, S. V., Er, P. X., Lawlor, K. T., Motazedian, A., Scurr, M., Ghobrial, I., Combes, A. N., Zappia, L., Oshlack, A., Stanley, E. G. & Little, M. H. Kidney micro-organoids in suspension culture as a scalable source of human pluripotent stem cell-derived kidney cells. *Development* **146**, doi:10.1242/dev.172361 (2019).

43 Avissar, N., Ornt, D. B., Yagil, Y., Horowitz, S., Watkins, R. H., Kerl, E. A., Takahashi, K., Palmer, I. S. & Cohen, H. J. Human kidney proximal tubules are the main source of plasma glutathione peroxidase. *Am J Physiol* **266**, C367-375, doi:10.1152/ajpcell.1994.266.2.C367 (1994).

990 44 Palacin, M., Fernandez, E., Chillaron, J. & Zorzano, A. The amino acid transport system
991 b(o,+) and cystinuria. *Mol Membr Biol* **18**, 21-26 (2001).

992 45 Schuh, C. D., Polesel, M., Platonova, E., Haenni, D., Gassama, A., Tokonami, N.,
993 Ghazi, S., Bugarski, M., Devuyst, O., Ziegler, U. & Hall, A. M. Combined Structural
994 and Functional Imaging of the Kidney Reveals Major Axial Differences in Proximal
995 Tubule Endocytosis. *J Am Soc Nephrol* **29**, 2696-2712, doi:10.1681/ASN.2018050522
996 (2018).

997 46 Verrey, F., Ristic, Z., Romeo, E., Ramadan, T., Makrides, V., Dave, M. H., Wagner, C.
998 A. & Camargo, S. M. Novel renal amino acid transporters. *Annu Rev Physiol* **67**, 557-
999 572, doi:10.1146/annurev.physiol.67.031103.153949 (2005).

1000 47 Fenollar-Ferrer, C., Forster, I. C., Patti, M., Knoepfel, T., Werner, A. & Forrest, L. R.
1001 Identification of the first sodium binding site of the phosphate cotransporter NaPi-IIa
1002 (SLC34A1). *Biophys J* **108**, 2465-2480, doi:10.1016/j.bpj.2015.03.054 (2015).

1003 48 Hummel, C. S., Lu, C., Loo, D. D., Hirayama, B. A., Voss, A. A. & Wright, E. M.
1004 Glucose transport by human renal Na+/D-glucose cotransporters SGLT1 and SGLT2.
1005 *Am J Physiol Cell Physiol* **300**, C14-21, doi:10.1152/ajpcell.00388.2010 (2011).

1006 49 Rahmoune, H., Thompson, P. W., Ward, J. M., Smith, C. D., Hong, G. & Brown, J.
1007 Glucose transporters in human renal proximal tubular cells isolated from the urine of
1008 patients with non-insulin-dependent diabetes. *Diabetes* **54**, 3427-3434,
1009 doi:10.2337/diabetes.54.12.3427 (2005).

1010 50 Wood, I. S. & Trayhurn, P. Glucose transporters (GLUT and SGLT): expanded families
1011 of sugar transport proteins. *Br J Nutr* **89**, 3-9, doi:10.1079/BJN2002763 (2003).

1012 51 Nagamori, S., Wiriyasermkul, P., Guarch, M. E., Okuyama, H., Nakagomi, S.,
1013 Tadagaki, K., Nishinaka, Y., Bodoy, S., Takafuji, K., Okuda, S., Kurokawa, J., Ohgaki,
1014 R., Nunes, V., Palacin, M. & Kanai, Y. Novel cystine transporter in renal proximal
1015 tubule identified as a missing partner of cystinuria-related plasma membrane protein
1016 rBAT/SLC3A1. *Proc Natl Acad Sci U S A* **113**, 775-780, doi:10.1073/pnas.1519959113
1017 (2016).

1018 52 Otsuka, M., Matsumoto, T., Morimoto, R., Arioka, S., Omote, H. & Moriyama, Y. A
1019 human transporter protein that mediates the final excretion step for toxic organic

cations. *Proc Natl Acad Sci U S A* **102**, 17923-17928, doi:10.1073/pnas.0506483102 (2005).

53 Vogetseder, A., Picard, N., Gaspert, A., Walch, M., Kaissling, B. & Le Hir, M. Proliferation capacity of the renal proximal tubule involves the bulk of differentiated epithelial cells. *Am J Physiol Cell Physiol* **294**, C22-28, doi:10.1152/ajpcell.00227.2007 (2008).

54 Nielsen, R., Christensen, E. I. & Birn, H. Megalin and cubilin in proximal tubule protein reabsorption: from experimental models to human disease. *Kidney Int* **89**, 58-67, doi:10.1016/j.kint.2015.11.007 (2016).

55 Kowalczuk, S., Broer, A., Tietze, N., Vanslambrouck, J. M., Rasko, J. E. & Broer, S. A protein complex in the brush-border membrane explains a Hartnup disorder allele. *FASEB J* **22**, 2880-2887, doi:fj.08-107300 [pii]

10.1096/fj.08-107300 (2008).

56 Kanai, Y., Fukasawa, Y., Cha, S. H., Segawa, H., Chairoungdua, A., Kim, D. K., Matsuo, H., Kim, J. Y., Miyamoto, K., Takeda, E. & Endou, H. Transport properties of a system y+L neutral and basic amino acid transporter. Insights into the mechanisms of substrate recognition. *J Biol Chem* **275**, 20787-20793, doi:10.1074/jbc.M000634200 (2000).

57 Verrey, F. System L: heteromeric exchangers of large, neutral amino acids involved in directional transport. *Pflugers Arch* **445**, 529-533, doi:10.1007/s00424-002-0973-z (2003).

58 Lee, J. W., Chou, C. L. & Knepper, M. A. Deep Sequencing in Microdissected Renal Tubules Identifies Nephron Segment-Specific Transcriptomes. *J Am Soc Nephrol* **26**, 2669-2677, doi:10.1681/ASN.2014111067 (2015).

59 Camargo, S. M., Singer, D., Makrides, V., Huggel, K., Pos, K. M., Wagner, C. A., Kuba, K., Danilczyk, U., Skovby, F., Kleta, R., Penninger, J. M. & Verrey, F. Tissue-specific amino acid transporter partners ACE2 and collectrin differentially interact with hartnup mutations. *Gastroenterology* **136**, 872-882, doi:10.1053/j.gastro.2008.10.055 (2009).

60 Fyfe, J. C., Madsen, M., Hojrup, P., Christensen, E. I., Tanner, S. M., de la Chapelle, A., He, Q. & Moestrup, S. K. The functional cobalamin (vitamin B12)-intrinsic factor receptor is a novel complex of cubilin and amnionless. *Blood* **103**, 1573-1579, doi:10.1182/blood-2003-08-2852 (2004).

61 Ahuja, R., Yammani, R., Bauer, J. A., Kalra, S., Seetharam, S. & Seetharam, B. Interactions of cubilin with megalin and the product of the amnionless gene (AMN): effect on its stability. *Biochem J* **410**, 301-308, doi:10.1042/BJ20070919 (2008).

62 Yasujima, T., Ohta, K. Y., Inoue, K., Ishimaru, M. & Yuasa, H. Evaluation of 4',6-diamidino-2-phenylindole as a fluorescent probe substrate for rapid assays of the functionality of human multidrug and toxin extrusion proteins. *Drug Metab Dispos* **38**, 715-721, doi:10.1124/dmd.109.030221 (2010).

63 Ozkok, A. & Edelstein, C. L. Pathophysiology of cisplatin-induced acute kidney injury. *Biomed Res Int* **2014**, 967826, doi:10.1155/2014/967826 (2014).

64 Yao, X., Panichpisal, K., Kurtzman, N. & Nugent, K. Cisplatin nephrotoxicity: a review. *Am J Med Sci* **334**, 115-124, doi:10.1097/MAJ.0b013e31812dfe1e (2007).

65 Abdelsalam, M., Elmorsy, E., Abdelwahab, H., Algohary, O., Naguib, M., El Wahab, A. A., Eldeeb, A., Eltoraby, E., Abdelsalam, A., Sabry, A., El-Metwally, M., Akl, M., Anber, N., El Sayed Zaki, M., Almutairi, F. & Mansour, T. Urinary biomarkers for early detection of platinum based drugs induced nephrotoxicity. *BMC Nephrol* **19**, 219, doi:10.1186/s12882-018-1022-2 (2018).

66 Chiusolo, A., Defazio, R., Zanetti, E., Mongillo, M., Mori, N., Cristofori, P. & Trevisan, A. Kidney injury molecule-1 expression in rat proximal tubule after treatment with segment-specific nephrotoxicants: a tool for early screening of potential kidney toxicity. *Toxicol Pathol* **38**, 338-345, doi:10.1177/0192623310362244 (2010).

67 Sasaki, D., Yamada, A., Umeno, H., Kurihara, H., Nakatsuji, S., Fujihira, S., Tsubota, K., Ono, M., Moriguchi, A., Watanabe, K. & Seki, J. Comparison of the course of biomarker changes and kidney injury in a rat model of drug-induced acute kidney injury. *Biomarkers* **16**, 553-566, doi:10.3109/1354750X.2011.613123 (2011).

68 Shinke, H., Masuda, S., Togashi, Y., Ikemi, Y., Ozawa, A., Sato, T., Kim, Y. H., Mishima, M., Ichimura, T., Bonventre, J. V. & Matsubara, K. Urinary kidney injury

molecule-1 and monocyte chemotactic protein-1 are noninvasive biomarkers of cisplatin-induced nephrotoxicity in lung cancer patients. *Cancer Chemother Pharmacol* **76**, 989-996, doi:10.1007/s00280-015-2880-y (2015).

69 Vaidya, V. S., Ozer, J. S., Dieterle, F., Collings, F. B., Ramirez, V., Troth, S., Muniappa, N., Thudium, D., Gerhold, D., Holder, D. J., Bobadilla, N. A., Marrer, E., Perentes, E., Cordier, A., Vonderscher, J., Maurer, G., Goering, P. L., Sistare, F. D. & Bonventre, J. V. Kidney injury molecule-1 outperforms traditional biomarkers of kidney injury in preclinical biomarker qualification studies. *Nature biotechnology* **28**, 478-485, doi:10.1038/nbt.1623 (2010).

70 Digby, J. L. M., Vanichapol, T., Przepiorski, A., Davidson, A. J. & Sander, V. Evaluation of cisplatin-induced injury in human kidney organoids. *Am J Physiol Renal Physiol* **318**, F971-F978, doi:10.1152/ajprenal.00597.2019 (2020).

71 Yoshimura, Y., Taguchi, A., Tanigawa, S., Yatsuda, J., Kamba, T., Takahashi, S., Kurihara, H., Mukoyama, M. & Nishinakamura, R. Manipulation of Nephron-Patterning Signals Enables Selective Induction of Podocytes from Human Pluripotent Stem Cells. *J Am Soc Nephrol* **30**, 304-321, doi:10.1681/ASN.2018070747 (2019).

72 Lescher, B., Haenig, B. & Kispert, A. sFRP-2 is a target of the Wnt-4 signaling pathway in the developing metanephric kidney. *Dev Dyn* **213**, 440-451, doi:10.1002/(SICI)1097-0177(199812)213:4<440::AID-AJA9>3.0.CO;2-6 (1998).

73 Yoshino, K., Rubin, J. S., Higinbotham, K. G., Uren, A., Anest, V., Plisov, S. Y. & Perantoni, A. O. Secreted Frizzled-related proteins can regulate metanephric development. *Mech Dev* **102**, 45-55, doi:10.1016/s0925-4773(01)00282-9 (2001).

74 Lawlor, K. T., Vanslambrouck, J. M., Higgins, J. W., Chambon, A., Bishard, K., Arndt, D., Er, P. X., Wilson, S. B., Howden, S. E., Tan, K. S., Li, F., Hale, L. J., Shepherd, B., Pentoney, S., Presnell, S. C., Chen, A. E. & Little, M. H. Cellular extrusion bioprinting improves kidney organoid reproducibility and conformation. *Nat Mater* **20**, 260-271, doi:10.1038/s41563-020-00853-9 (2021).

75 Cruz, N. M., Song, X., Czerniecki, S. M., Gulieva, R. E., Churchill, A. J., Kim, Y. K., Winston, K., Tran, L. M., Diaz, M. A., Fu, H., Finn, L. S., Pei, Y., Himmelfarb, J. & Freedman, B. S. Organoid cystogenesis reveals a critical role of microenvironment in

human polycystic kidney disease. *Nat Mater* **16**, 1112-1119, doi:10.1038/nmat4994 (2017).

76 Forbes, T. A., Howden, S. E., Lawlor, K., Phipson, B., Maksimovic, J., Hale, L., Wilson, S., Quinlan, C., Ho, G., Holman, K., Bennetts, B., Crawford, J., Trnka, P., Oshlack, A., Patel, C., Mallett, A., Simons, C. & Little, M. H. Patient-iPSC-Derived Kidney Organoids Show Functional Validation of a Ciliopathic Renal Phenotype and Reveal Underlying Pathogenetic Mechanisms. *Am J Hum Genet* **102**, 816-831, doi:10.1016/j.ajhg.2018.03.014 (2018).

77 Hale, L. J., Howden, S. E., Phipson, B., Lonsdale, A., Er, P. X., Ghobrial, I., Hosawi, S., Wilson, S., Lawlor, K. T., Khan, S., Oshlack, A., Quinlan, C., Lennon, R. & Little, M. H. 3D organoid-derived human glomeruli for personalised podocyte disease modelling and drug screening. *Nature communications* **9**, 5167, doi:10.1038/s41467-018-07594-z (2018).

78 Hollywood, J. A., Przepiorski, A., D'Souza, R. F., Sreebhavan, S., Wolvetang, E. J., Harrison, P. T., Davidson, A. J. & Holm, T. M. Use of Human Induced Pluripotent Stem Cells and Kidney Organoids To Develop a Cysteamine/mTOR Inhibition Combination Therapy for Cystinosis. *J Am Soc Nephrol* **31**, 962-982, doi:10.1681/ASN.2019070712 (2020).

79 Mae, S., Shono, A., Shiota, F., Yasuno, T., Kajiwara, M., Gotoda-Nishimura, N., Arai, S., Sato-Otubo, A., Toyoda, T., Takahashi, K., Nakayama, N., Cowan, C. A., Aoi, T., Ogawa, S., McMahon, A. P., Yamanaka, S. & Osafune, K. Monitoring and robust induction of nephrogenic intermediate mesoderm from human pluripotent stem cells. *Nature communications* **4**, 1367, doi:10.1038/ncomms2378 (2013).

80 Przepiorski, A., Sander, V., Tran, T., Hollywood, J. A., Sorrenson, B., Shih, J. H., Wolvetang, E. J., McMahon, A. P., Holm, T. M. & Davidson, A. J. A Simple Bioreactor-Based Method to Generate Kidney Organoids from Pluripotent Stem Cells. *Stem Cell Reports* **11**, 470-484, doi:10.1016/j.stemcr.2018.06.018 (2018).

81 Taguchi, A. & Nishinakamura, R. Higher-Order Kidney Organogenesis from Pluripotent Stem Cells. *Cell Stem Cell* **21**, 730-746 e736, doi:10.1016/j.stem.2017.10.011 (2017).

82 Tanigawa, S., Islam, M., Sharmin, S., Naganuma, H., Yoshimura, Y., Haque, F., Era, T., Nakazato, H., Nakanishi, K., Sakuma, T., Yamamoto, T., Kurihara, H., Taguchi, A. & Nishinakamura, R. Organoids from Nephrotic Disease-Derived iPSCs Identify Impaired NEPHRIN Localization and Slit Diaphragm Formation in Kidney Podocytes. *Stem Cell Reports* **11**, 727-740, doi:10.1016/j.stemcr.2018.08.003 (2018).

83 Han, L., Wei, X., Liu, C., Volpe, G., Wang, Z., Pan, T., Yuan, Y., Lei, Y., Lai, Y., Ward, C., Yu, Y., Wang, M., Shi, Q., Wu, T., Wu, L., Liu, Y., Wang, C., Zhang, Y., Sun, H., Yu, H., Zhuang, Z., Tang, T., Huang, Y., Lu, H., Xu, L., Xu, J., Cheng, M., Liu, Y., Wong, C. W., Tan, T., Ji, W., Maxwell, P. H., Yang, H., Wang, J., Zhu, S., Liu, S., Xu, X., Hou, Y., Esteban, M. A., Liu, L. & Consortium, S. C. G. B. A.-S. C. Single-cell atlas of a non-human primate reveals new pathogenic mechanisms of COVID-19. 2020.2004.2010.022103, doi:10.1101/2020.04.10.022103 %J bioRxiv (2020).

84 Marchiano, S., Hsiang, T. Y., Khanna, A., Higashi, T., Whitmore, L. S., Bargehr, J., Davaapil, H., Chang, J., Smith, E., Ong, L. P., Colzani, M., Reinecke, H., Yang, X., Pabon, L., Sinha, S., Najafian, B., Sniadecki, N. J., Bertero, A., Gale, M., Jr. & Murry, C. E. SARS-CoV-2 Infects Human Pluripotent Stem Cell-Derived Cardiomyocytes, Impairing Electrical and Mechanical Function. *Stem Cell Reports* **16**, 478-492, doi:10.1016/j.stemcr.2021.02.008 (2021).

85 Mills, R. J., Humphrey, S. J., Fortuna, P. R. J., Lor, M., Foster, S. R., Quaife-Ryan, G. A., Johnston, R. L., Dumenil, T., Bishop, C., Rudraraju, R., Rawle, D. J., Le, T., Zhao, W., Lee, L., Mackenzie-Kludas, C., Mehdiabadi, N. R., Halliday, C., Gilham, D., Fu, L., Nicholls, S. J., Johansson, J., Sweeney, M., Wong, N. C. W., Kulikowski, E., Sokolowski, K. A., Tse, B. W. C., Devilee, L., Voges, H. K., Reynolds, L. T., Krumeich, S., Mathieson, E., Abu-Bonsrah, D., Karavendzas, K., Griffen, B., Titmarsh, D., Elliott, D. A., McMahon, J., Suhrbier, A., Subbarao, K., Porrello, E. R., Smyth, M. J., Engwerda, C. R., MacDonald, K. P. A., Bald, T., James, D. E. & Hudson, J. E. BET inhibition blocks inflammation-induced cardiac dysfunction and SARS-CoV-2 infection. *Cell* **184**, 2167-2182 e2122, doi:10.1016/j.cell.2021.03.026 (2021).

86 Sharma, A., Garcia, G., Jr., Wang, Y., Plummer, J. T., Morizono, K., Arumugaswami, V. & Svendsen, C. N. Human iPSC-Derived Cardiomyocytes Are Susceptible to SARS-CoV-2 Infection. *Cell Rep Med* **1**, 100052, doi:10.1016/j.xcrm.2020.100052 (2020).

87 Tiwari, S. K., Wang, S., Smith, D., Carlin, A. F. & Rana, T. M. Revealing Tissue-Specific SARS-CoV-2 Infection and Host Responses using Human Stem Cell-Derived Lung and Cerebral Organoids. *Stem Cell Reports* **16**, 437-445, doi:10.1016/j.stemcr.2021.02.005 (2021).

88 Huang, C., Wang, Y., Li, X., Ren, L., Zhao, J., Hu, Y., Zhang, L., Fan, G., Xu, J., Gu, X., Cheng, Z., Yu, T., Xia, J., Wei, Y., Wu, W., Xie, X., Yin, W., Li, H., Liu, M., Xiao, Y., Gao, H., Guo, L., Xie, J., Wang, G., Jiang, R., Gao, Z., Jin, Q., Wang, J. & Cao, B. Clinical features of patients infected with 2019 novel coronavirus in Wuhan, China. *Lancet* **395**, 497-506, doi:10.1016/S0140-6736(20)30183-5 (2020).

89 Kunutsor, S. K. & Laukkanen, J. A. Renal complications in COVID-19: a systematic review and meta-analysis. *Ann Med* **52**, 345-353, doi:10.1080/07853890.2020.1790643 (2020).

90 Yang, X., Yu, Y., Xu, J., Shu, H., Xia, J., Liu, H., Wu, Y., Zhang, L., Yu, Z., Fang, M., Yu, T., Wang, Y., Pan, S., Zou, X., Yuan, S. & Shang, Y. Clinical course and outcomes of critically ill patients with SARS-CoV-2 pneumonia in Wuhan, China: a single-centered, retrospective, observational study. *Lancet Respir Med* **8**, 475-481, doi:10.1016/S2213-2600(20)30079-5 (2020).

91 Zhou, F., Yu, T., Du, R., Fan, G., Liu, Y., Liu, Z., Xiang, J., Wang, Y., Song, B., Gu, X., Guan, L., Wei, Y., Li, H., Wu, X., Xu, J., Tu, S., Zhang, Y., Chen, H. & Cao, B. Clinical course and risk factors for mortality of adult inpatients with COVID-19 in Wuhan, China: a retrospective cohort study. *Lancet* **395**, 1054-1062, doi:10.1016/S0140-6736(20)30566-3 (2020).

92 Monteil, V., Kwon, H., Prado, P., Hagelkruys, A., Wimmer, R. A., Stahl, M., Leopoldi, A., Garreta, E., Hurtado Del Pozo, C., Prosper, F., Romero, J. P., Wirnsberger, G., Zhang, H., Slutsky, A. S., Conder, R., Montserrat, N., Mirazimi, A. & Penninger, J. M. Inhibition of SARS-CoV-2 Infections in Engineered Human Tissues Using Clinical-Grade Soluble Human ACE2. *Cell* **181**, 905-913 e907, doi:10.1016/j.cell.2020.04.004 (2020).

93 Wysocki, J., Ye, M., Hassler, L., Gupta, A. K., Wang, Y., Nicoleascu, V., Randall, G., Wertheim, J. A. & Batlle, D. A Novel Soluble ACE2 Variant with Prolonged Duration

of Action Neutralizes SARS-CoV-2 Infection in Human Kidney Organoids. *J Am Soc Nephrol*, doi:10.1681/ASN.2020101537 (2021).

94 Motavalli, R., Abdelbasset, W. K., Rahman, H. S., Achmad, M. H., Sergeevna, N. K., Zekiy, A. O., Adili, A., Khiavi, F. M., Marofi, F., Yousefi, M., Ghoreishizadeh, S., Shomali, N., Etemadi, J. & Jarahian, M. The lethal internal face of the coronaviruses: Kidney tropism of the SARS, MERS, and COVID19 viruses. *IUBMB Life* **73**, 1005-1015, doi:10.1002/iub.2516 (2021).

95 Hoffmann, M., Kleine-Weber, H., Schroeder, S., Kruger, N., Herrler, T., Erichsen, S., Schiergens, T. S., Herrler, G., Wu, N. H., Nitsche, A., Muller, M. A., Drosten, C. & Pohlmann, S. SARS-CoV-2 Cell Entry Depends on ACE2 and TMPRSS2 and Is Blocked by a Clinically Proven Protease Inhibitor. *Cell* **181**, 271-280 e278, doi:10.1016/j.cell.2020.02.052 (2020).

96 Braun, F., Lutgehetmann, M., Pfefferle, S., Wong, M. N., Carsten, A., Lindenmeyer, M. T., Norz, D., Heinrich, F., Meissner, K., Wichmann, D., Kluge, S., Gross, O., Pueschel, K., Schroder, A. S., Edler, C., Aepfelbacher, M., Puelles, V. G. & Huber, T. B. SARS-CoV-2 renal tropism associates with acute kidney injury. *Lancet* **396**, 597-598, doi:10.1016/S0140-6736(20)31759-1 (2020).

97 Farkash, E. A., Wilson, A. M. & Jentzen, J. M. Ultrastructural Evidence for Direct Renal Infection with SARS-CoV-2. *J Am Soc Nephrol* **31**, 1683-1687, doi:10.1681/ASN.2020040432 (2020).

98 Kissling, S., Rotman, S., Gerber, C., Halfon, M., Lamoth, F., Comte, D., Lhopitallier, L., Sadallah, S. & Fakhouri, F. Collapsing glomerulopathy in a COVID-19 patient. *Kidney Int* **98**, 228-231, doi:10.1016/j.kint.2020.04.006 (2020).

99 Puelles, V. G., Lutgehetmann, M., Lindenmeyer, M. T., Sperhake, J. P., Wong, M. N., Allweiss, L., Chilla, S., Heinemann, A., Wanner, N., Liu, S., Braun, F., Lu, S., Pfefferle, S., Schroder, A. S., Edler, C., Gross, O., Glatzel, M., Wichmann, D., Wiech, T., Kluge, S., Pueschel, K., Aepfelbacher, M. & Huber, T. B. Multiorgan and Renal Tropism of SARS-CoV-2. *N Engl J Med* **383**, 590-592, doi:10.1056/NEJMc2011400 (2020).

100 Su, H., Yang, M., Wan, C., Yi, L. X., Tang, F., Zhu, H. Y., Yi, F., Yang, H. C., Fogo, A. B., Nie, X. & Zhang, C. Renal histopathological analysis of 26 postmortem findings

of patients with COVID-19 in China. *Kidney Int* **98**, 219-227, doi:10.1016/j.kint.2020.04.003 (2020).

101 Werion, A., Belkhir, L., Perrot, M., Schmit, G., Aydin, S., Chen, Z., Penaloza, A., De Greef, J., Yildiz, H., Pothen, L., Yombi, J. C., Dewulf, J., Scohy, A., Gerard, L., Wittebole, X., Laterre, P. F., Miller, S. E., Devuyst, O., Jadoul, M., Morelle, J. & Cliniques universitaires Saint-Luc, C.-R. G. SARS-CoV-2 causes a specific dysfunction of the kidney proximal tubule. *Kidney Int* **98**, 1296-1307, doi:10.1016/j.kint.2020.07.019 (2020).

102 Hanley, B., Naresh, K. N., Roufosse, C., Nicholson, A. G., Weir, J., Cooke, G. S., Thursz, M., Manousou, P., Corbett, R., Goldin, R., Al-Sarraj, S., Abdolrasouli, A., Swann, O. C., Baillon, L., Penn, R., Barclay, W. S., Viola, P. & Osborn, M. Histopathological findings and viral tropism in UK patients with severe fatal COVID-19: a post-mortem study. *Lancet Microbe* **1**, e245-e253, doi:10.1016/S2666-5247(20)30115-4 (2020).

103 Amraei, R., Yin, W., Napoleon, M. A., Suder, E. L., Berrigan, J., Zhao, Q., Olejnik, J., Chandler, K. B., Xia, C., Feldman, J., Hauser, B. M., Caradonna, T. M., Schmidt, A. G., Gummuluru, S., Muhlberger, E., Chitalia, V., Costello, C. E. & Rahimi, N. CD209L/L-SIGN and CD209/DC-SIGN act as receptors for SARS-CoV-2. *bioRxiv*, doi:10.1101/2020.06.22.165803 (2021).

104 Singh, M., Bansal, V. & Feschotte, C. A Single-Cell RNA Expression Map of Human Coronavirus Entry Factors. *Cell reports* **32**, 108175, doi:10.1016/j.celrep.2020.108175 (2020).

105 Kuppe, C., Leuchtle, K., Wagner, A., Kabgani, N., Saritas, T., Puelles, V. G., Smeets, B., Hakroush, S., van der Vlag, J., Boor, P., Schiffer, M., Grone, H. J., Fogo, A., Floege, J. & Moeller, M. J. Novel parietal epithelial cell subpopulations contribute to focal segmental glomerulosclerosis and glomerular tip lesions. *Kidney Int* **96**, 80-93, doi:10.1016/j.kint.2019.01.037 (2019).

106 Wang, M. Not your usual parietal cell. *Nature reviews. Nephrology* **15**, 318, doi:10.1038/s41581-019-0141-8 (2019).

107 Broer, S., Bailey, C. G., Kowalczuk, S., Ng, C., Vanslambrouck, J. M., Rodgers, H., Auray-Blais, C., Cavanaugh, J. A., Broer, A. & Rasko, J. E. Iminoglycinuria and

hyperglycinuria are discrete human phenotypes resulting from complex mutations in proline and glycine transporters. *J Clin Invest* **118**, 3881-3892, doi:10.1172/JCI36625 36625 [pii] (2008).

108 van Dijk, D., Sharma, R., Nainys, J., Yim, K., Kathail, P., Carr, A. J., Burdziak, C., Moon, K. R., Chaffer, C. L., Pattabiraman, D., Bierie, B., Mazutis, L., Wolf, G., Krishnaswamy, S. & Pe'er, D. Recovering Gene Interactions from Single-Cell Data Using Data Diffusion. *Cell* **174**, 716-729 e727, doi:10.1016/j.cell.2018.05.061 (2018).

109 Boyle, S. C., Kim, M., Valerius, M. T., McMahon, A. P. & Kopan, R. Notch pathway activation can replace the requirement for Wnt4 and Wnt9b in mesenchymal-to-epithelial transition of nephron stem cells. *Development* **138**, 4245-4254, doi:10.1242/dev.070433 (2011).

110 Chung, E., Deacon, P. & Park, J. S. Notch is required for the formation of all nephron segments and primes nephron progenitors for differentiation. *Development* **144**, 4530-4539, doi:10.1242/dev.156661 (2017).

111 Surendran, K., Boyle, S., Barak, H., Kim, M., Stomberski, C., McCright, B. & Kopan, R. The contribution of Notch1 to nephron segmentation in the developing kidney is revealed in a sensitized Notch2 background and can be augmented by reducing Mint dosage. *Dev Biol* **337**, 386-395, doi:10.1016/j.ydbio.2009.11.017 (2010).

112 Karner, C. M., Das, A., Ma, Z., Self, M., Chen, C., Lum, L., Oliver, G. & Carroll, T. J. Canonical Wnt9b signaling balances progenitor cell expansion and differentiation during kidney development. *Development* **138**, 1247-1257, doi:10.1242/dev.057646 (2011).

113 Park, J. S., Valerius, M. T. & McMahon, A. P. Wnt/beta-catenin signaling regulates nephron induction during mouse kidney development. *Development* **134**, 2533-2539, doi:10.1242/dev.006155 (2007).

114 Blank, U., Brown, A., Adams, D. C., Karolak, M. J. & Oxburgh, L. BMP7 promotes proliferation of nephron progenitor cells via a JNK-dependent mechanism. *Development* **136**, 3557-3566, doi:10.1242/dev.036335 (2009).

115 Lindstrom, N. O., Carragher, N. O. & Hohenstein, P. The PI3K pathway balances self-renewal and differentiation of nephron progenitor cells through beta-catenin signaling. *Stem Cell Reports* **4**, 551-560, doi:10.1016/j.stemcr.2015.01.021 (2015).

116 Muthukrishnan, S. D., Yang, X., Friesel, R. & Oxburgh, L. Concurrent BMP7 and FGF9 signalling governs AP-1 function to promote self-renewal of nephron progenitor cells. *Nature communications* **6**, 10027, doi:10.1038/ncomms10027 (2015).

117 Tanigawa, S., Naganuma, H., Kaku, Y., Era, T., Sakuma, T., Yamamoto, T., Taguchi, A. & Nishinakamura, R. Activin Is Superior to BMP7 for Efficient Maintenance of Human iPSC-Derived Nephron Progenitors. *Stem Cell Reports* **13**, 322-337, doi:10.1016/j.stemcr.2019.07.003 (2019).

118 Lindstrom, N. O., Hohenstein, P. & Davies, J. A. Nephrons require Rho-kinase for proximal-distal polarity development. *Sci Rep* **3**, 2692, doi:10.1038/srep02692 (2013).

119 Barasch, J., Yang, J., Ware, C. B., Taga, T., Yoshida, K., Erdjument-Bromage, H., Tempst, P., Parravicini, E., Malach, S., Aranoff, T. & Oliver, J. A. Mesenchymal to epithelial conversion in rat metanephros is induced by LIF. *Cell* **99**, 377-386 (1999).

120 Bard, J. B. & Ross, A. S. LIF, the ES-cell inhibition factor, reversibly blocks nephrogenesis in cultured mouse kidney rudiments. *Development* **113**, 193-198 (1991).

121 Matsuda, M., Hayashi, H., Garcia-Ojalvo, J., Yoshioka-Kobayashi, K., Kageyama, R., Yamanaka, Y., Ikeya, M., Toguchida, J., Alev, C. & Ebisuya, M. Species-specific segmentation clock periods are due to differential biochemical reaction speeds. *Science* **369**, 1450-1455, doi:10.1126/science.aba7668 (2020).

122 Lancaster, M. A., Renner, M., Martin, C. A., Wenzel, D., Bicknell, L. S., Hurles, M. E., Homfray, T., Penninger, J. M., Jackson, A. P. & Knoblich, J. A. Cerebral organoids model human brain development and microcephaly. *Nature* **501**, 373-379, doi:10.1038/nature12517 (2013).

123 Velasco, S., Kedaigle, A. J., Simmons, S. K., Nash, A., Rocha, M., Quadrato, G., Paulsen, B., Nguyen, L., Adiconis, X., Regev, A., Levin, J. Z. & Arlotta, P. Individual brain organoids reproducibly form cell diversity of the human cerebral cortex. *Nature* **570**, 523-527, doi:10.1038/s41586-019-1289-x (2019).

124 Bantounas, I., Silajdzic, E., Woolf, A. S. & Kimber, S. J. Formation of Mature Nephrons by Implantation of Human Pluripotent Stem Cell-Derived Progenitors into Mice. *Methods in molecular biology* **2067**, 309-322, doi:10.1007/978-1-4939-9841-8_19 (2020).

125 Nam, S. A., Seo, E., Kim, J. W., Kim, H. W., Kim, H. L., Kim, K., Kim, T. M., Ju, J. H., Gomez, I. G., Uchimura, K., Humphreys, B. D., Yang, C. W., Lee, J. Y., Kim, J., Cho, D. W., Freedman, B. S. & Kim, Y. K. Graft immaturity and safety concerns in transplanted human kidney organoids. *Exp Mol Med* **51**, 1-13, doi:10.1038/s12276-019-0336-x (2019).

126 van den Berg, C. W., Ritsma, L., Avramut, M. C., Wiersma, L. E., van den Berg, B. M., Leuning, D. G., Lievers, E., Koning, M., Vanslambrouck, J. M., Koster, A. J., Howden, S. E., Takasato, M., Little, M. H. & Rabelink, T. J. Renal Subcapsular Transplantation of PSC-Derived Kidney Organoids Induces Neo-vasculogenesis and Significant Glomerular and Tubular Maturation In Vivo. *Stem Cell Reports* **10**, 751-765, doi:10.1016/j.stemcr.2018.01.041 (2018).

127 Silhol, F., Sarlon, G., Deharo, J. C. & Vaisse, B. Downregulation of ACE2 induces overstimulation of the renin-angiotensin system in COVID-19: should we block the renin-angiotensin system? *Hypertens Res* **43**, 854-856, doi:10.1038/s41440-020-0476-3 (2020).

128 Reddy, R., Asante, I., Liu, S., Parikh, P., Liebler, J., Borok, Z., Rodgers, K., Baydur, A. & Louie, S. G. Circulating angiotensin peptides levels in Acute Respiratory Distress Syndrome correlate with clinical outcomes: A pilot study. *PLoS One* **14**, e0213096, doi:10.1371/journal.pone.0213096 (2019).

129 Diaz, J. H. Hypothesis: angiotensin-converting enzyme inhibitors and angiotensin receptor blockers may increase the risk of severe COVID-19. *J Travel Med* **27**, doi:10.1093/jtm/taaa041 (2020).

130 Esler, M. & Esler, D. Can angiotensin receptor-blocking drugs perhaps be harmful in the COVID-19 pandemic? *J Hypertens* **38**, 781-782, doi:10.1097/HJH.0000000000002450 (2020).

131 Fang, L., Karakiulakis, G. & Roth, M. Are patients with hypertension and diabetes mellitus at increased risk for COVID-19 infection? *Lancet Respir Med* **8**, e21, doi:10.1016/S2213-2600(20)30116-8 (2020).

132 Hippisley-Cox, J., Young, D., Coupland, C., Channon, K. M., Tan, P. S., Harrison, D. A., Rowan, K., Aveyard, P., Pavord, I. D. & Watkinson, P. J. Risk of severe COVID-19 disease with ACE inhibitors and angiotensin receptor blockers: cohort study including 8.3 million people. *Heart* **106**, 1503-1511, doi:10.1136/heartjnl-2020-317393 (2020).

133 Li, M., Wang, Y., Ndiwane, N., Orner, M. B., Palacios, N., Mittler, B., Berlowitz, D., Kazis, L. E. & Xia, W. The association of COVID-19 occurrence and severity with the use of angiotensin converting enzyme inhibitors or angiotensin-II receptor blockers in patients with hypertension. *PLoS One* **16**, e0248652, doi:10.1371/journal.pone.0248652 (2021).

134 Vaduganathan, M., Vardeny, O., Michel, T., McMurray, J. J. V., Pfeffer, M. A. & Solomon, S. D. Renin-Angiotensin-Aldosterone System Inhibitors in Patients with Covid-19. *N Engl J Med* **382**, 1653-1659, doi:10.1056/NEJMsr2005760 (2020).

135 Herrera, S., Bernal-Maurandi, J., Cofan, F., Ventura, P., Marcos, M. A., Linares, L., Cuesta, G., Diekmann, F., Moreno, A. & Bodro, M. BK Virus and Cytomegalovirus Coinfections in Kidney Transplantation and Their Impact on Allograft Loss. *J Clin Med* **10**, doi:10.3390/jcm10173779 (2021).

136 Schutgens, F., Rookmaaker, M. B., Margaritis, T., Rios, A., Ammerlaan, C., Jansen, J., Gijzen, L., Vormann, M., Vonk, A., Viveen, M., Yengej, F. Y., Derakhshan, S., de Winter-de Groot, K. M., Artegiani, B., van Boxtel, R., Cuppen, E., Hendrickx, A. P. A., van den Heuvel-Eibrink, M. M., Heitzer, E., Lanz, H., Beekman, J., Murk, J. L., Masereeuw, R., Holstege, F., Drost, J., Verhaar, M. C. & Clevers, H. Tubuloids derived from human adult kidney and urine for personalized disease modeling. *Nature biotechnology* **37**, 303-313, doi:10.1038/s41587-019-0048-8 (2019).

137 Briggs, J. A., Sun, J., Shepherd, J., Ovchinnikov, D. A., Chung, T. L., Nayler, S. P., Kao, L. P., Morrow, C. A., Thakar, N. Y., Soo, S. Y., Peura, T., Grimmond, S. & Wolvetang, E. J. Integration-free induced pluripotent stem cells model genetic and

neural developmental features of down syndrome etiology. *Stem Cells* **31**, 467-478, doi:10.1002/stem.1297 (2013).

138 Vlahos, K., Sourris, K., Mayberry, R., McDonald, P., Bruveris, F. F., Schiesser, J. V., Bozaoglu, K., Lockhart, P. J., Stanley, E. G. & Elefanty, A. G. Generation of iPSC lines from peripheral blood mononuclear cells from 5 healthy adults. *Stem Cell Res* **34**, 101380, doi:10.1016/j.scr.2018.101380 (2019).

139 Chen, G., Gulbranson, D. R., Hou, Z., Bolin, J. M., Ruotti, V., Probasco, M. D., Smuga-Otto, K., Howden, S. E., Diol, N. R., Propson, N. E., Wagner, R., Lee, G. O., Antosiewicz-Bourget, J., Teng, J. M. & Thomson, J. A. Chemically defined conditions for human iPSC derivation and culture. *Nat Methods* **8**, 424-429, doi:10.1038/nmeth.1593 (2011).

140 Schindelin, J., Arganda-Carreras, I., Frise, E., Kaynig, V., Longair, M., Pietzsch, T., Preibisch, S., Rueden, C., Saalfeld, S., Schmid, B., Tinevez, J. Y., White, D. J., Hartenstein, V., Eliceiri, K., Tomancak, P. & Cardona, A. Fiji: an open-source platform for biological-image analysis. *Nat Methods* **9**, 676-682, doi:10.1038/nmeth.2019 (2012).

141 Stoeckius, M., Zheng, S., Houck-Loomis, B., Hao, S., Yeung, B. Z., Mauck, W. M., 3rd, Smibert, P. & Satija, R. Cell Hashing with barcoded antibodies enables multiplexing and doublet detection for single cell genomics. *Genome Biol* **19**, 224, doi:10.1186/s13059-018-1603-1 (2018).

142 Ransick, A., Lindstrom, N. O., Liu, J., Zhu, Q., Guo, J. J., Alvarado, G. F., Kim, A. D., Black, H. G., Kim, J. & McMahon, A. P. Single-Cell Profiling Reveals Sex, Lineage, and Regional Diversity in the Mouse Kidney. *Developmental cell* **51**, 399-413 e397, doi:10.1016/j.devcel.2019.10.005 (2019).

143 Hafemeister, C. & Satija, R. Normalization and variance stabilization of single-cell RNA-seq data using regularized negative binomial regression. *Genome Biol* **20**, 296, doi:10.1186/s13059-019-1874-1 (2019).

144 Butler, A., Hoffman, P., Smibert, P., Papalexi, E. & Satija, R. Integrating single-cell transcriptomic data across different conditions, technologies, and species. *Nature biotechnology* **36**, 411-420, doi:10.1038/nbt.4096 (2018).

145 Stuart, T., Butler, A., Hoffman, P., Hafemeister, C., Papalexi, E., Mauck, W. M., 3rd, Hao, Y., Stoeckius, M., Smibert, P. & Satija, R. Comprehensive Integration of Single-Cell Data. *Cell* **177**, 1888-1902 e1821, doi:10.1016/j.cell.2019.05.031 (2019).

Figures and legends

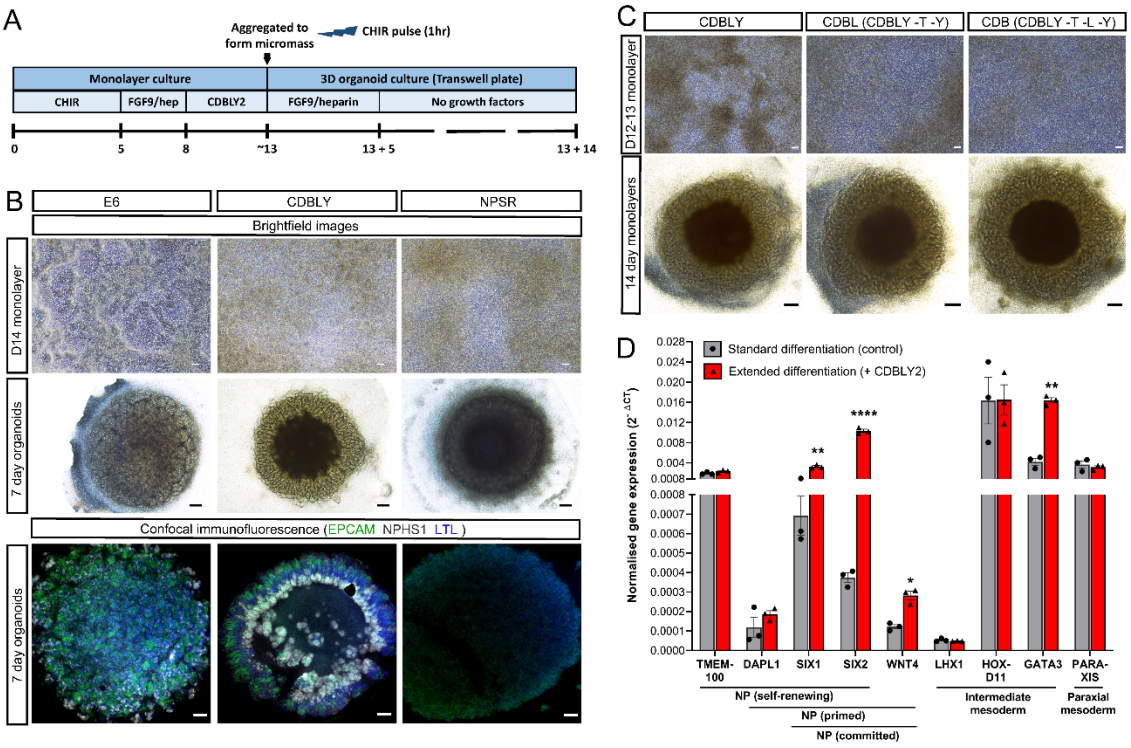

Figure 1: Extended monolayer culture in CDBLY supports nephron progenitors and preserves nephrogenic capacity. A. Schematic depicting the extended differentiation protocol in CDBLY2. **B.** Brightfield and confocal immunofluorescence images of extended monolayer differentiations in E6, CDBLY and NPSR, and resulting organoids. Immunofluorescence depicts nephrons (EPCAM; green), podocytes of glomeruli (NPHS1; grey), and proximal tubules (LTL; blue). Scale bars represent 100µm (monolayers) and 200µm (organoids). **C.** Brightfield images of extended monolayer differentiations using CDBLY variations and resulting organoids. Scale bars represent 100µm (monolayers) and 200µm (organoids). **D.** qRT-PCR analysis of standard and extended monolayer differentiations. Error bars represent SEM from n = 3 biological replicates. Statistical significance was determined using an unpaired t test. Asterisks represent P values adjusted for multiple comparisons using the Holm-Sidak method, alpha = 0.05 (*; $P \leq 0.05$, **; $P \leq 0.01$, ***; $P \leq 0.001$, ****; $P \leq 0.0001$).

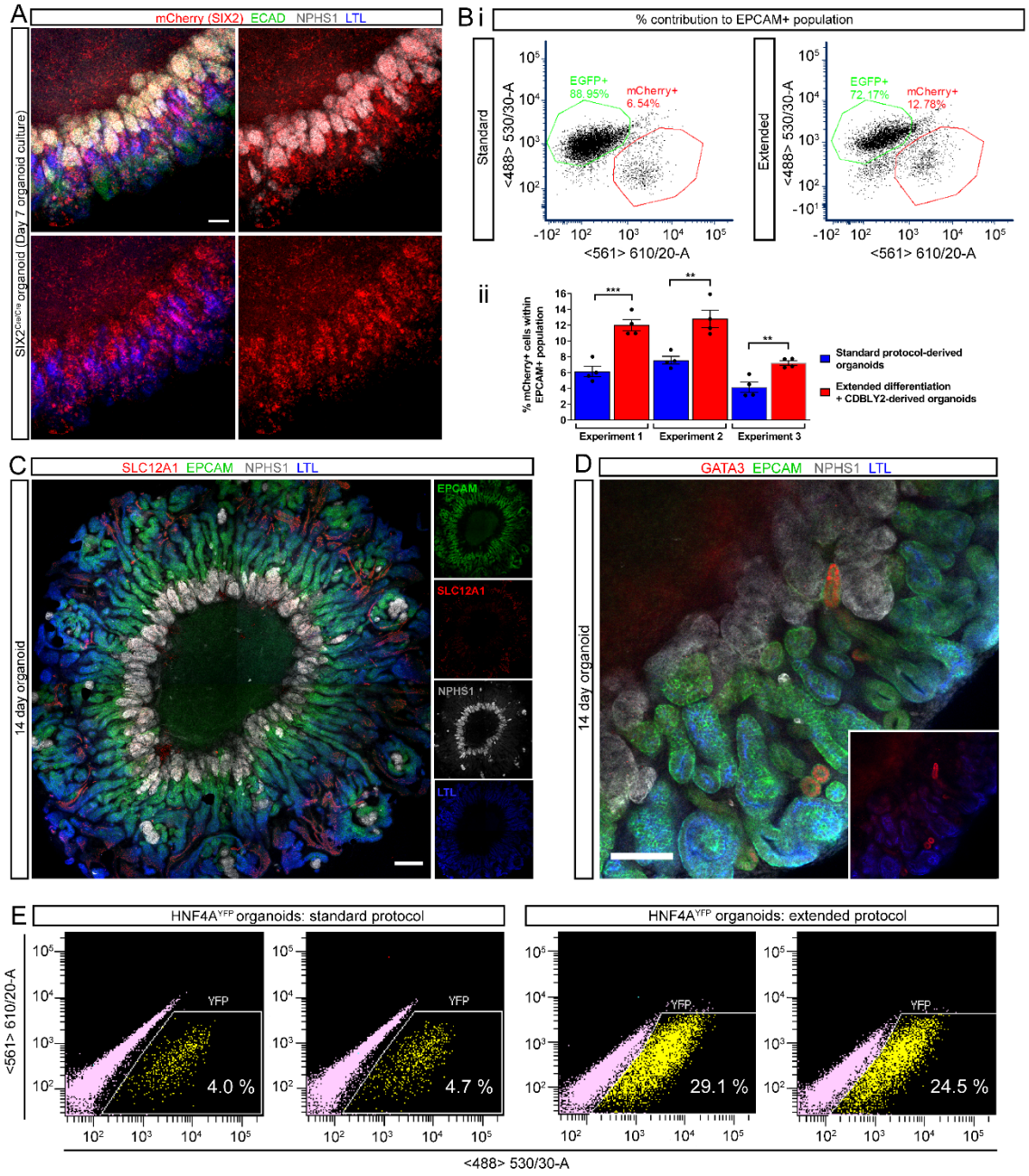

Figure 2: Extended monolayer culture in CDBLY2 increases SIX2+ progenitor contribution to nephrons and proximalisation. A. Confocal immunofluorescence of D14 + 7 organoid derived from the SIX2^{Cre} lineage tracing iPSC line. Images depict merged and separated channels showing lineage-traced SIX2+ cells (mCherry; red), distal tubules (ECAD; green), podocytes (NPHS1; grey) and proximal tubules (LTL; blue). Scale bar represents 100 µm. **B.** Flow cytometry of SIX2$^{Cre/Cre}$:GAPDH^{dual} lineage tracing organoids derived from extended (13 day + CDBLY2) and standard (7 day + E6 media) differentiations depicting mCherry contribution to the EPCAM+ (nephron) population. Flow plots shown in (i) are representative of the replicates across multiple experiments. Percentage mCherry contributions

from flow cytometry are depicted in bar graph (ii). Error bars in (ii) represent SEM from n = 4 biological replicates across 3 independent experiments. Statistical significance was determined using an unpaired t test. Asterisks represent P values adjusted for multiple comparisons using the Holm-Sidak method, alpha = 0.05 (*; $P \leq 0.05$, **; $P \leq 0.01$, ***; $P \leq 0.001$, ****; $P \leq 0.0001$). **C.** Confocal immunofluorescence of a D13+14 organoid demonstrating aligned nephron morphology as well as nephron segmentation makers; nephron epithelium (EpCAM; green), distal tubule/Loop of Henle (SLC12A1; red), proximal tubules (LTL; blue), and podocytes (NPHS1; grey). Scale bar represents 200 µm. **C**. Confocal immunofluorescence of a D13+14 organoid demonstrating few GATA3+ (connecting segment/ureteric epithelium; red) cells, co-stained for nephron epithelium (EPCAM; green), podocytes (NPHS1; grey), and proximal tubules (LTL; blue). Inset shows GATA3 and LTL alone. Scale bar represents 100 µm. **D.** Flow cytometry of representative $HNF4A^{YFP}$ derived organoids generated using the extended differentiation + CDBLY2 protocol (generating PT-enhanced organoids) or the standard organoid protocol.

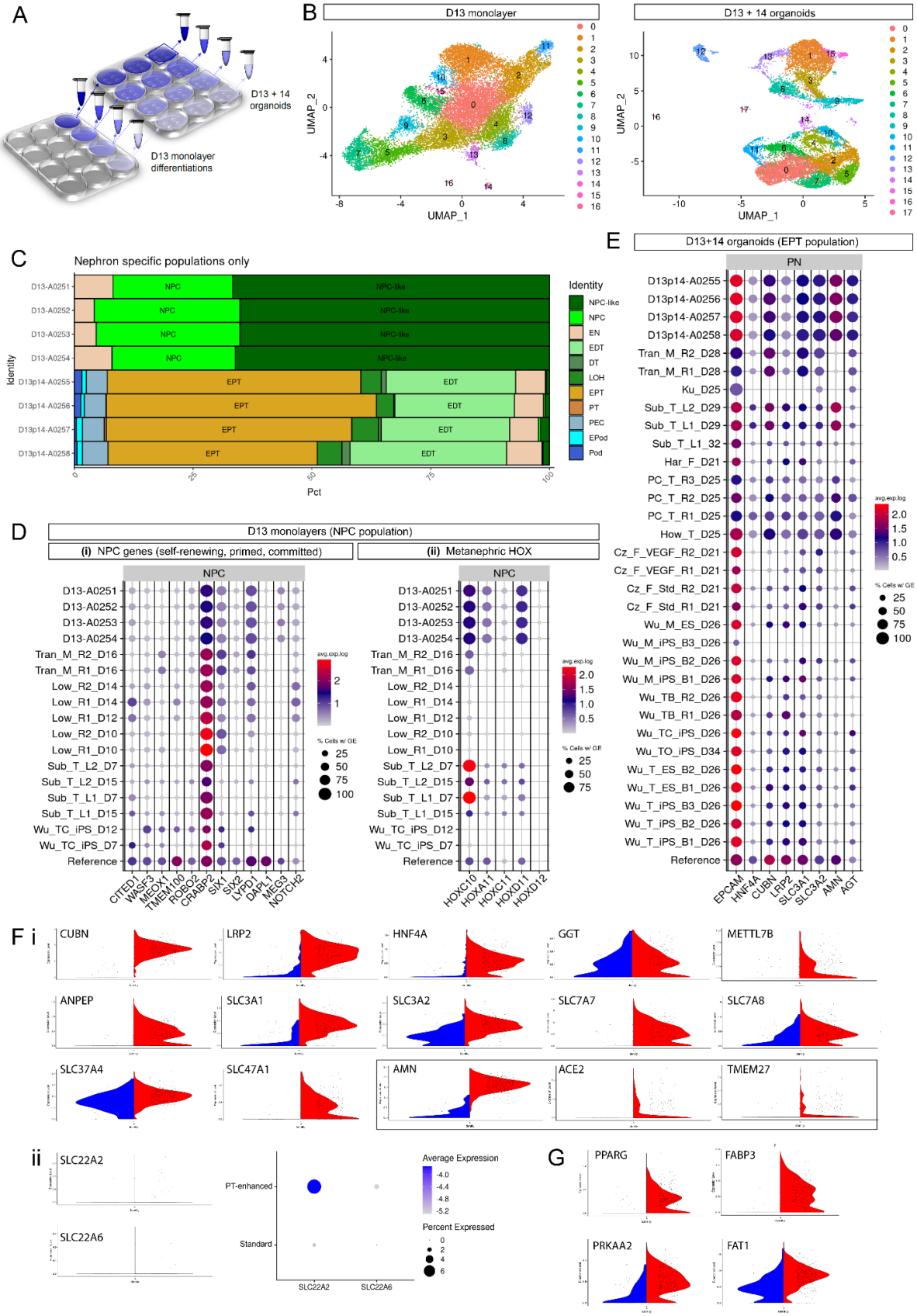

Figure 3: Single cell transcriptional profiling (scRNAseq) shows improved specification, patterning and maturation of proximal tubules and their progenitors. A. Schematic

depicting experimental design and profiled samples. Multiple organoids (2.5 x 10^5 cells per organoid) were generated from each of the 4 replicate differentiated cell monolayers at D13. The remaining portion of cells from each replicate monolayer were barcoded and pooled for generation of the D13 monolayer library. The resulting organoids were cultured for 14 days before being harvested and pooled within replicate wells, making 4 cell suspensions. These 4 suspensions were individually barcoded and pooled into a single cell suspension for generation of the D13+14 organoid library. **B.** UMAP plots of D13 and D13+14 samples (pooled replicates) identifying 16 and 17 distinct cell clusters, respectively. **C.** *ComparePlots* depicting proportions of kidney cell types (nephron-specific populations only) in D13 and D13+14 sample replicates as classified by *DevKidCC*. Population abbreviations: nephron progenitor cell (NPC), early nephron (EN), early distal tubule (EDT), DT (distal tubule), loop of Henle (LOH), early proximal tubule (EPT), proximal tubule (PT), parietal epithelial cell (PEC), early podocyte (EPod), podocyte (Pod). **D.** *DevKidCC* dot plots comparing the expression of gene signatures for (**i**) self-renewing (*SIX1, SIX2, CITED1, WASF3, DAPL1, MEOX1, TMEM100, ROBO2, CRABP2*), committed (*SIX1, SIX2, LYPD1*), and primed (*DAPL1, NOTCH2, MEG3*) NPC subsets, as well as (**ii**) metanephric HOX genes, within the D13 monolayer NPC population to that of published stem cell-derived kidney datasets and a mixed (week 11 – 18) human fetal kidney reference dataset (Hochane*, et al.*, 2019; Tran*, et al.*, 2019; Hollywood*, et al.*, 2020). Comparisons were made to published monolayer and early nephrogenic datasets (Subramanian*, et al.*, 2019; Wu*, et al.*, 2018; Low*, et al.*, 2019; Tran*, et al.*, 2019) as outlined previously (Wilson*, et al.*, 2021) . **E.** *DevKidCC* dot plot comparing the expression of proximal nephron (PN) gene signatures within the EPT population of D13+14 organoids to that of published stem cell-derived kidney organoid datasets (Czerniecki*, et al.*, 2018; Harder*, et al.*, 2019; Kumar*, et al.*, 2019) and the mixed week 11 - 18 fetal kidney reference dataset (Hochane*, et al.*, 2019; Tran*, et al.*, 2019; Hollywood*, et al.*, 2020) as outlined previously(Wilson*, et al.*, 2021). **F.** Violin plots in (**i**) and (**ii**) compare PT-specific gene expression between line- and age-matched standard (blue) and PT-enhanced (red) organoids. Genes encoding auxiliary proteins around outlined (bottom row). Violin plots for *SLC22A2* and *SLC22A6* are redisplayed as dot plots in (**ii**). **G**. Violin plots comparing examples of genes involved in fatty acid metabolism in line- and age-matched standard (blue) and PT-enhanced (red) organoids.

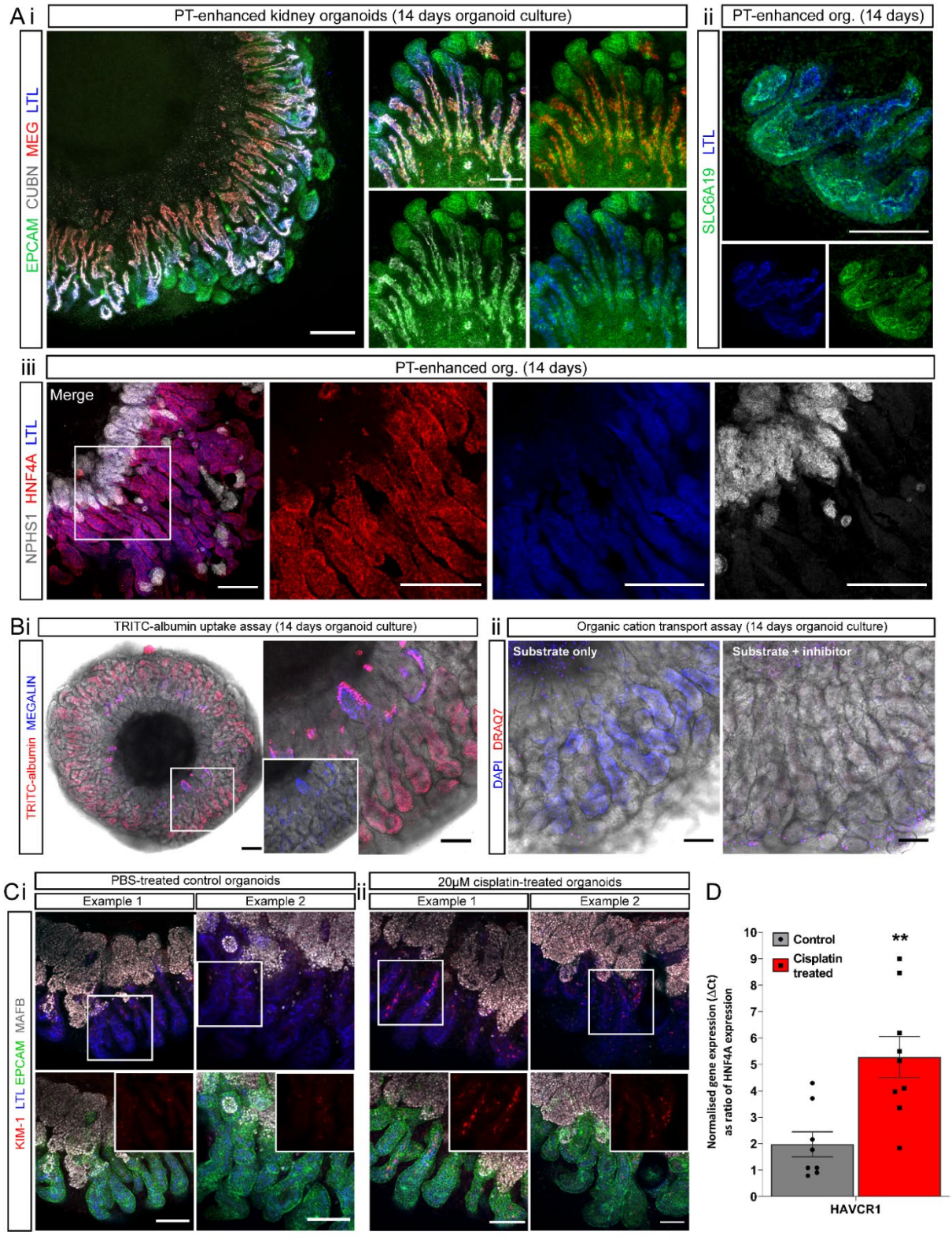

Figure 4: PT-enhanced organoids express mature and functional PT transporters and transcription factors at a protein level. A. Confocal immunofluorescence of PT markers within EPCAM+ (green) nephrons in D13+14 PT-enhanced kidney, including (Ai) LTL (blue), CUBILIN (CUBN; grey), MEGALIN (MEG; red), (Aii) SLC6A19 (green), and (Aiii) HNF4A

(red). Podocytes (Aiii) are marked by NPHS1 (grey). Scale bars in (Ai) and (Aiii) represent 200µm. Scale bar in (Aii) represents 100µm. **Bi.** Confocal images of live organoids under phase-contrast depicting uptake of TRITC-albumin (red) into MEGALIN-positive PTs (blue). Outlined area of whole organoid image (left) is shown at higher magnification on right panel. Inset (right panel) depicts MEGALIN (blue) staining alone. Scale bars represent 200µm (left) and 100µm (right). **Bii.** Confocal images of live organoids under phase-contrast depicting DAPI uptake as a surrogate for organic cation transport capacity. Left and right panels show organoids exposed to substrate (DAPI; blue) alone and to a combination of substrate and inhibitor (Cimetidine), respectively. Dead cells in both panels are labelled with DRAQ7 (red). Scale bars represent 100µm. **C.** Confocal immunofluorescence of representative D13+14 organoids following 24 hours treatment with E6 media containing either 20µM cisplatin (Cii) or an equivalent volume of PBS (Ci). Images depict KIM-1-expressing cells (red) in LTL+ proximal tubules (blue) with nephron epithelium marked by EPCAM (green). Insets show red channel (KIM-1) alone. Scale bars represent 100µm. **D**. qRT-PCR analysis of D13+14 control and cisplatin-treated organoids from (**C**). Error bars represent SEM from n = 8 (control) and n = 9 (cisplatin treated) biological replicates across 3 independent experiments. Statistical significance was determined using an unpaired t test. Asterisk represents P value (**; $P \leq 0.01$) adjusted for multiple comparisons using the Holm-Sidak method, alpha = 0.05.

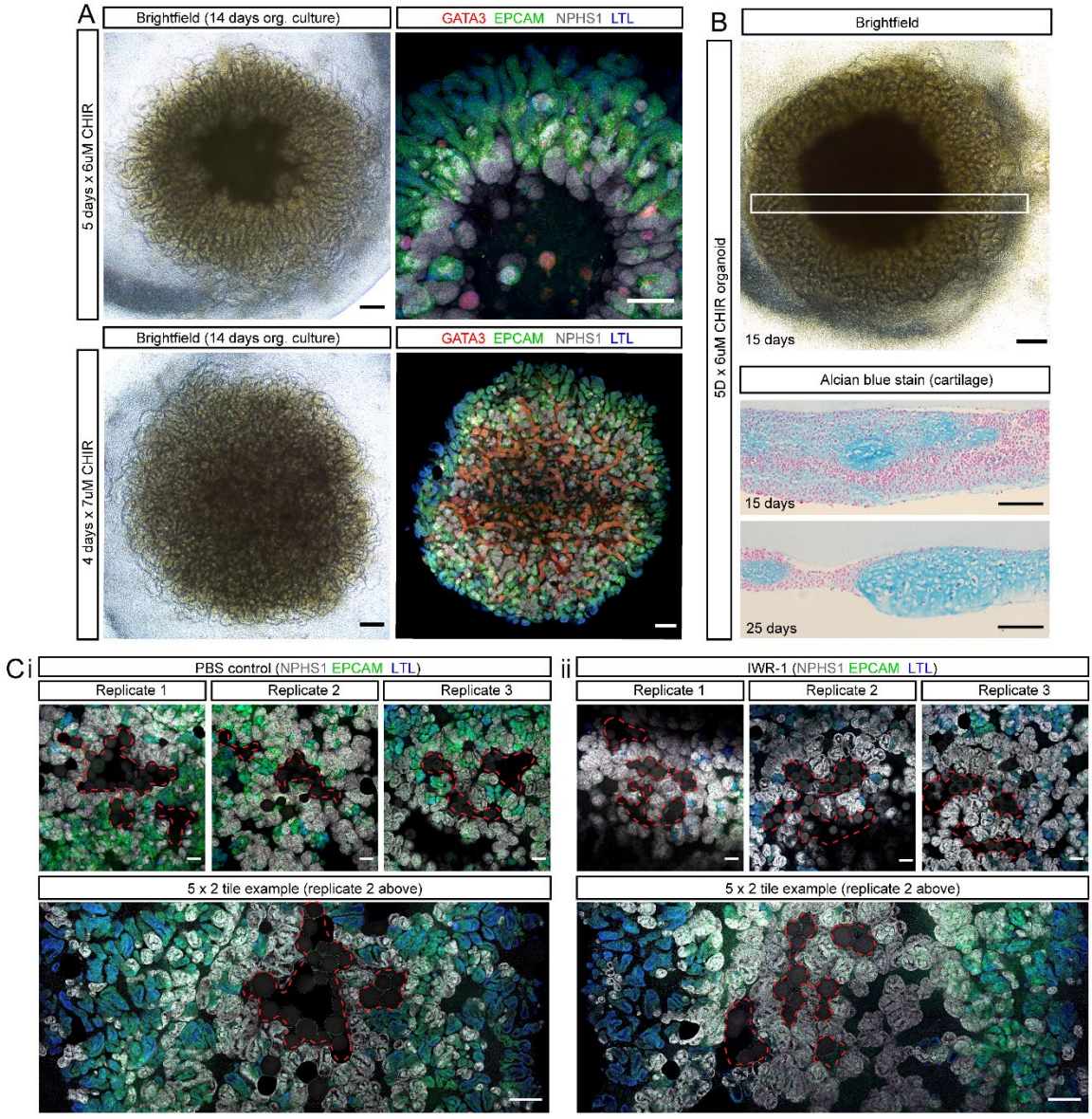

Figure 5. WNT signalling gradient influences nephron alignment and directionality. A. Brightfield and confocal immunofluorescence images of organoids derived from 13 days of extended monolayer culture in CDBLY2, with varying initial CHIR exposure conditions during first 7 days. Bottom panels depict nephron segmentation markers; nephron epithelium (EpCAM; green), ureteric epithelium/connecting segment (GATA3; red), proximal tubules (LTL; blue), and podocytes (NPHS1; grey). Scale bar represents 200 µm. **B.** Representative brightfield image (top) of a day 13+15 organoid exposed to 5 days x 6µM CHIR prior to CDBLY2 addition at monolayer differentiation day 8. White box indicates approximate regions of cross sections shown in bottom panels stained with Alcian blue to indicate cartilage formation in central core region (blue). Scale bars represent 200 µm. **C.** Confocal immunofluorescence images of replicate standard organoids bioprinted in a patch conformation

1522 and in contact with either agarose beads soaked PBS (control; Di) or in 10μM IWR-1 (Dii).
1523 Clusters of beads are outlined with red dashed lines. Organoids are stained with markers of
1524 epithelium (EPCAM; green), proximal tubule (LTL; blue), and podocytes of the glomeruli
1525 (NPHS1; grey). Scale bars represent 100 μm (all top panels) and 200 μm (bottom tile panels).

1526

1527

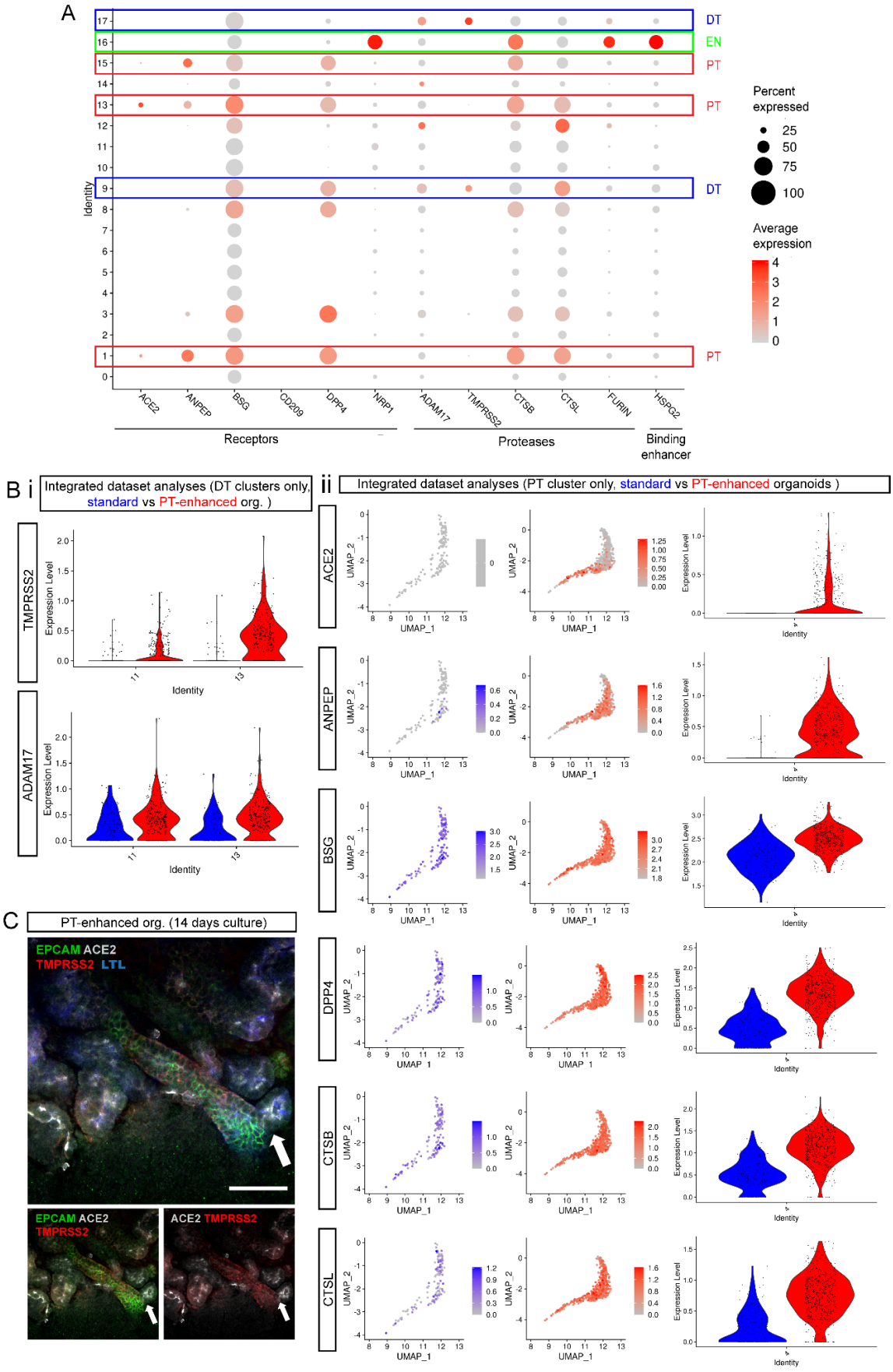

Figure 6: PT-enhanced organoids show improved SARS-CoV-2 entry factor expression.

A. scRNASeq analysis of SARS-CoV-2 entry factor expression in D13+14 kidney organoids. Boxes outline proximal (red), distal (blue), and endothelial (green) clusters. **B.** scRNASeq analysis of SARS-CoV-2 entry factor expression in age- and line- matched standard (blue) and PT-enhanced (red) (D13+12) kidney organoids. Feature plots and violin plots compare expression of genes within integrated datasets from which distal tubule (DT; Bi) and proximal tubule (PT; Bii) clusters have been isolated. **C.** Confocal immunofluorescence of ACE2 (green) and TMPRSS2 (red) demonstrating protein localisation in PT-enhanced kidney organoids. Nephron epithelium is stained with EPCAM (green). Entry factors, ACE2 and TMPRSS2, are depicted in grey and red, while arrow indicates a section of continuous nephron epithelium with distinctly separate ACE2 and TMPRSS2 expression. Scale bars represent 50μm.

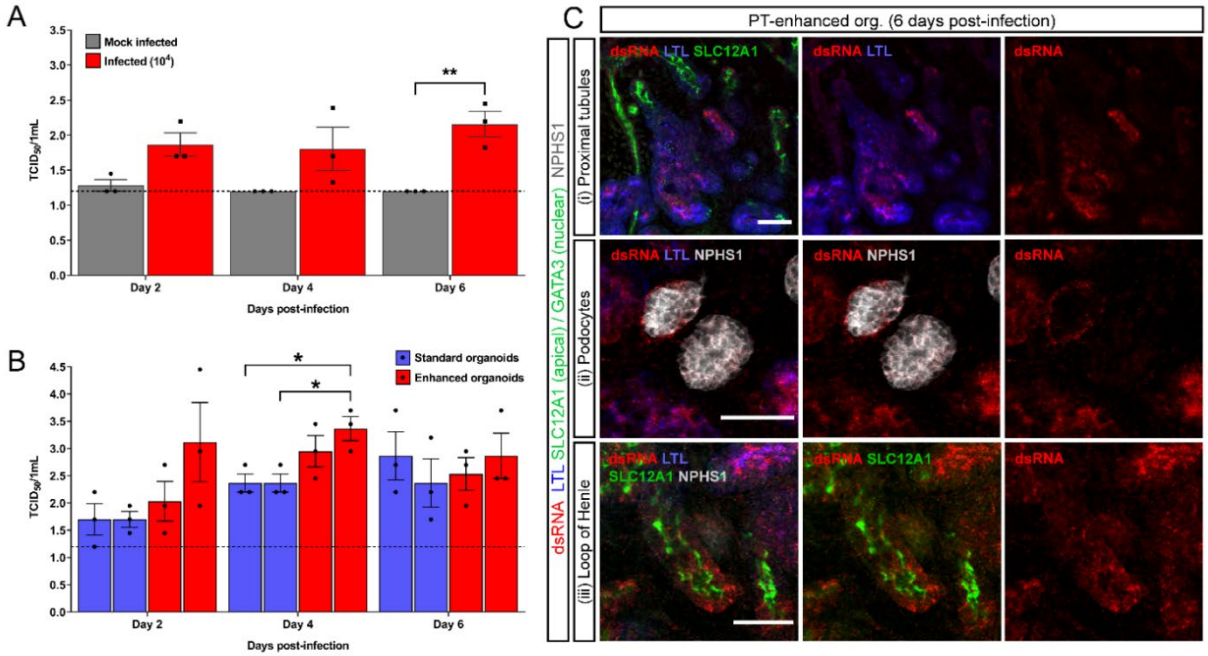

Figure 7: PT-enhanced organoids show evidence of SARS-CoV-2 infection and improved viral replication. A. Virus titre expressed as median Tissue Culture Infectious Dose ($TCID_{50}$) of SARS-CoV-2-infected (red bars) and mock-infected (grey bars) PT-enhanced organoids. Dotted line represents lower limit of detection (LOD). Error bars represent SEM from n = 3 independent experiments infecting 2 – 4 wells per experiment (3 organoids per well) . Statistical significance was determined using an unpaired t test. Asterisk represents P value adjusted for multiple comparisons using the Holm-Sidak method, alpha = 0.05 (*; $P \leq 0.05$, **; $P \leq 0.01$, ***; $P \leq 0.001$, ****; $P \leq 0.0001$). **B.** Virus titre in SARS-CoV-2-infected standard organoids (blue bars) and PT-enhanced organoids (red bars). Dotted line represents lower limit of detection (LOD). Error bars represent SEM from n = 3 wells (3 organoids per well) across independent experiments replicated using the same iPSC line and organoid conditions. Statistical significance was determined using a two-way ANOVA with Geisser-Greenhouse correction and uncorrected Fisher's LSD (individual variances computed for each comparison). Asterisks represent P values (*; $P \leq 0.05$, **; $P \leq 0.01$, ***; $P \leq 0.001$, ****; $P \leq 0.0001$). **C.** Confocal immunofluorescence of PT-enhanced organoids 6 days post-infection indicating viral dsRNA (red) localisation, co-stained for PTs (LTL; blue), Loop of Henle (SLC12A1; apical green), and podocytes (NPHS1; grey). Scale bars represent 50µm.